Generation of the Early Cretaceous granitoid in the Dazeshan region, Jiaodong Peninsula: Implications for the crustal reworking in the North China Craton

Leilei Dong[1]*, Zhiming Yang[1,2], Xin Bai[1] and Chen Deng[3]

[1]School of Civil and Resource Engineering, University of Science and Technology Beijing, Beijing, China, [2]Institute of Geology, Chinese Academy of Geological Sciences, Beijing, China, [3]Postdoctoral Programme, Guosen Securities, Shenzhen, China

Lower crust-derived granitic rocks provide constraints on the crustal reworking process and consequently give hints on the destruction mechanism of the cratons. The North China Craton (NCC) underwent extensive crustal melting in the Mesozoic. This study investigated granitic intrusions in the Dazeshan region of the Jiaodong Peninsula. Whole-rock major and trace element analyses and zircon U-Pb ages coupled with Hf isotopes were used to reveal the crustal reworking processes. Zircons separated from the quartz porphyry, Linglong granite, rhyolite porphyry, and biotite granite showed weighted mean ^{206}Pb-^{238}U ages of 119.2 ± 1.0 Ma, 140.2 ± 1.0 Ma, 120.6 ± 0.5 Ma, and 119.9 ± 0.7 Ma, respectively. The quartz porphyry, rhyolite porphyry, and biotite granite had high silica contents (SiO_2 = 74–77 wt.%) but low MgO, Co, and Ni concentrations. The calculated $\varepsilon_{Hf}(t)$ values for the rhyolite porphyry and the biotite granite ranged from −18.3 to −20.0 and −17.8 to −20.2, respectively. These geochemical features imply ancient crust sources. The quartz porphyry showed distinct primitive mantle-normalized rare earth element (REE) patterns and was characterized by lower ΣREE content and lack of pronounced negative Eu anomalies. Whole-rock and zircon Dy/Yb ratios showed no correlation with whole-rock Rb/Sr ratios and zircon Hf contents, reflecting limited effects of crystal fractionation. The Ba/La ratios were also high (>150), but the Sr/Y and La/Yb ratios were low (Sr/Y < 50; La/Yb < 15). These features likely indicate that the quartz porphyry was generated by water-fluxed melting without differentiation. The rhyolite porphyry and biotite granite shared many geochemical similarities, denoting a unified source. The high La/Yb (>30) but low Sr/Y (<20) ratios and apparent negative Eu anomalies indicated plagioclase fractionation. Decreased zircon Dy/Yb with increasing Hf concentrations reflected noticeable amphibole fractionation. These two suites had fairly low Ba/La ratios. These data together point toward an identical source: dehydration melting of a relatively thickened crust. These melts experienced crystal fractionation after extraction. We propose that the intrusions were generated by the underplating of water-rich mafic magma, which provided both fluid and heat and finally induced two kinds of melting.

1 Introduction

Cratons are generally considered the most stable part of the lithosphere because the great thickness of the continental mantle beneath cratons prevents them from being destroyed by the convective mantle. However, decades of research have greatly improved our understanding and we now know that stable cratons can be destroyed (Gao et al., 2004; Xu et al., 2009; Lee et al., 2011; Wu et al., 2019). The NCC has stabilized following the amalgamation between the western and eastern blocks at about 1.9 Ga (Zhao et al., 2005). However, it was reworked during the Mesozoic and the thick lithosphere underwent extensive thinning, particularly at the eastern part of the NCC (Menzies et al., 2007; Chen et al., 2008; Wu et al., 2019). The destruction of NCC was accompanied by crustal reworking and the development of extensional structures and many metamorphic core complexes (like the Gudaoling and Linglong) and sedimentary basins (Charles et al., 2012; Meng et al., 2019; Wu et al., 2019; Zheng and Gao, 2021). Thus, these processes are used as indicators of decratonization in the NCC.

This thinning process of the lithosphere mantle can be traced at the shallow crustal levels by Jurassic-Cretaceous granitic rocks, as they represent thermal or tectonic disturbances underneath the thick crust (Chappell, 2004; Weinberg and Hasalová, 2015; Gao et al., 2016; Zheng and Gao, 2021). Although extensive studies have been conducted on these magmatic rocks to demonstrate the timing and mechanisms of NCC destruction, some divergences exist regarding the timing and duration of the NCC destruction. The onset of NCC destruction remains elusive because the understanding of "destruction" differs (Xu et al., 2009). The northern and southern margins of the NCC were subducted by the Paleo-Asian Oceanic slab and the South China Block during the Carboniferous-Permian and Late Triassic, respectively (Windley et al., 2010). The resultant magmatism in the northern and southern margins indicated changes in lithospheric structure and thermal structure. Following this logic, the NCC destruction initiated in different craton margins in the Carboniferous and Triassic (Xu et al., 2009). Nevertheless, the destruction of NCC is now broadly recognized to have peaked in the Early Cretaceous (Wu et al., 2005a), as indicated by extensive granitic magmatism associated with mantle-crust interactions.

The mechanism of lithosphere thinning also remains under debate. One school of thought argues that the thinning occurs mechanically by delamination (Gao et al., 2004; Ma et al., 2014), while other researchers believe that the thinning proceeds gradually *via* a thermal-chemical erosion process (Xu et al., 2009; Geng et al., 2019). Hou et al. (2007) inferred that the ~130 Ma Guojialing suite adakitic granitoids were formed by crustal thickening during the descent into the asthenosphere

(delamination). Ma et al. (2014) proposed that the lithosphere mantle was rapidly replaced by the fertile asthenosphere mantle at ca. 120 Ma by delamination based on investigations of the mafic dykes in Jiaodong. These results drive the timing of delamination, if it occurred, towards later times. Therefore, the genesis of these Early Cretaceous magmatic rocks is crucial for understanding the crustal evolution of the NCC. However, how these granitic rocks were generated remains undetermined in the NCC (e.g., fluid fluxed or dehydration melting), particularly those magmatic rocks formed at ca. 120 Ma. This impedes our knowledge of decratonization processes. This study investigated the petrogenesis of the granitic rocks that intruded into the Jurassic Linglong granite in the Dazeshan region in Jiaodong Penisular, to reveal the crustal reworking processes.

2 Geological background

The Jiaodong Penisular is an integral part of the NCC, which has Early Archean crustal remnants (Jahn and Zhang, 1984; Liu et al., 1992). The NCC was stabilized through the amalgamation of the eastern and western blocks during a Paleoproterozoic orogenic event along the Trans-North China Orogen (Figure 1) (Zhao, 2001). Both blocks are dominated by Late Archaean tonalitic–trondhjemitic–granodioritic (TTG) gneiss complexes with minor supracrustal rocks with metamorphic ages of ~2.5 Ga (Zhao, 2001). The Jiaodong Penisula is located in the southeastern part of the NCC and was displaced to its current location by the approximately 2,400 km Tanlu fault (Zhu et al., 2009). Three main tectonic units constitute the Jiaodong Peninsula: the Jiaobei terrane, the Sulu orogen, and the Jiaolai basin (Figure 1).

The Jiaobei terrane, an integral part of the NCC, comprises Archean-Paleozoic metamorphic rocks and TTG gneiss (such as biotite gneiss and plagioclase amphibolite). These rock units are mainly located in the Qixia area. The Jurassic Linglong granite, along with the Luanjianhe and Biguo granites, intrudes into the Precambrian rocks and together constitute the composite Linglong pluton (Figure 1). The zircon U-Pb ages of this composite pluton range from 170 to 150 Ma (Yang et al., 2012; Yang et al., 2017). The volumetrically smaller Guojialing, Congjia, Beijie, and Shangzhuang granodiorite were subsequently emplaced during the Early Cretaceous. The zircon U-Pb ages of these plutonic rocks range from 130 to 127 Ma (Yang et al., 2012; Jiang et al., 2016). The Aishan and Nansu porphyry granites, which feature large K-feldspar phenosrysts, are emplaced within the Guojialing granodiorite and the Linglong granite, respectively, and have zircon U-Pb ages of 118–116 Ma (Goss et al., 2010; Li et al., 2012). The Sulu orogen

FIGURE 1
(A) Geological map of the Jiaodong Peninsula, showing major structures, lithological units, and study area (Song et al., 2021). **(B)** The U-Pb ages obtained in this study are noted on the map.
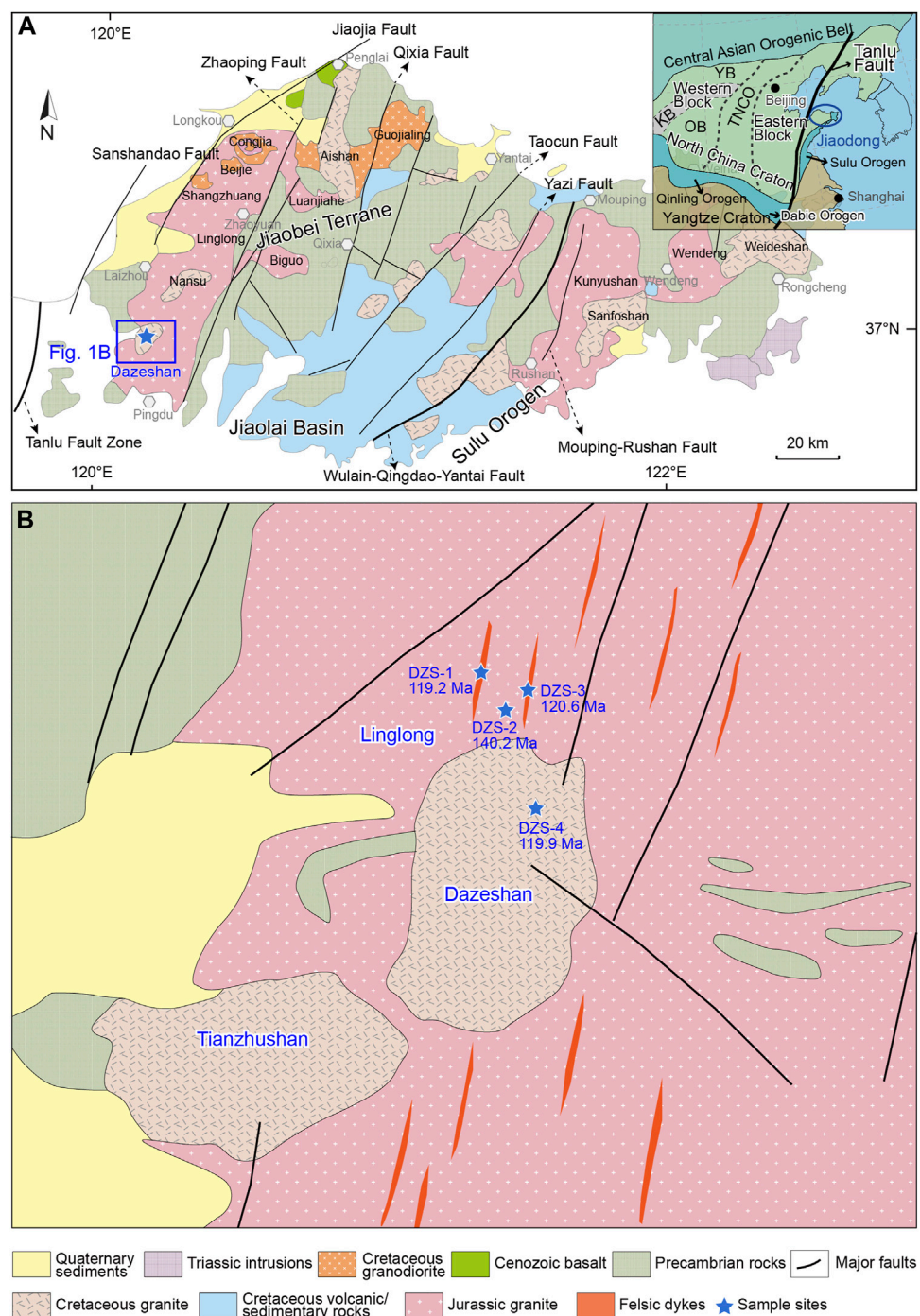
is situated to the east of the Wulian-Qingdao-Yantai fault and is considered the suture zone separating the NCC and South China Block (Wu and Zheng, 2013). Many ultrahigh- to high-pressure metamorphic rocks are preserved in the Sulu orogen.

Additionally, the Triassic alkaline complex in the Rongcheng area (Shidao) dates to 225–205 Ma and represents magmatism related to mantle upwelling after continent-continent collision (Chen et al., 2003). The Jiaolai basin comprises volcanic and
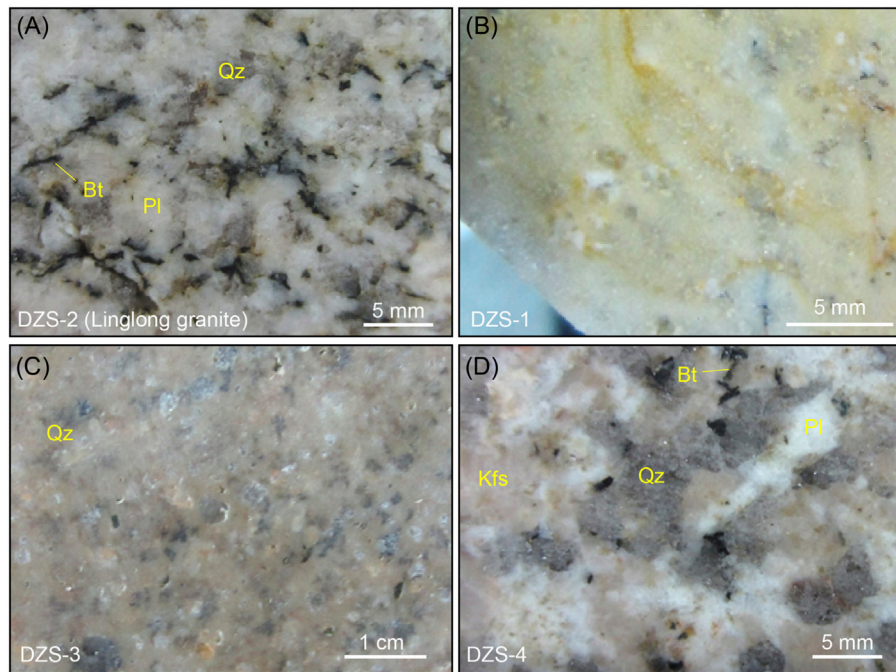
FIGURE 2
(A–D) Photographs of Linglong granite, quartz porphyry, rhyolite porphyry, and Dazeshan biotite granite.
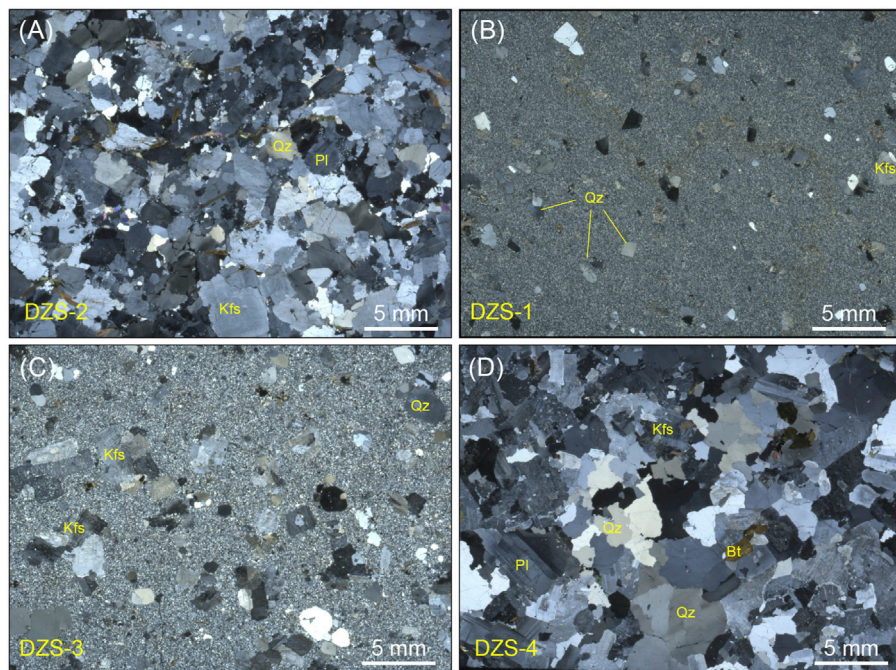
FIGURE 3
Microscopic images of Linglong granite **(A)**, quartz porphyry **(B)**, rhyolite porphyry **(C),** and Dazeshan biotite granite **(D)**. Abbreviations: Kfs = K-feldspar, Pl = plagioclase, Qz = quartz, Bt = biotite. The abbreviations for the minerals are after Whitney and Evans. (2010).

sedimentary sequences deposited in the Early Cretaceous (Zhang et al., 2008). The main volcanic rocks in the Jiaolai basin are Qingshan group basic to felsic rocks, including rhyolite, andesite, dacite, and tuff. Laiyang and Wangshi group sedimentary rocks (sandstone and mudstone) cover the Qingshan group volcanic rocks. Cenozoic basalt, although rarely exposed, is mainly reported in the Penglai area (Figure 1).

3 Samples and analytical methods

The samples investigated in this study were collected in the Dazeshan region at the Jiaobei terrane (Figure 1B). Four types of magmatic rocks were sampled: quartz porphyry (DZS-1), Linglong granite (DZS-2), rhyolite porphyry (DZS-3), and Dazeshan biotite granite (DZS-4) (Figure 2). From field observations, the quartz porphyry, rhyolite porphyry, and Dazeshan biotite granite all intruded the Linglong granite. The Linglong granite is predominantly composed of plagioclase, K-feldspar, quartz, and biotite (Figures 2A, 3A). The sizes of the plagioclase, K-feldspar, and quartz are similar (2–5 mm). The biotite crystals are smaller and appear to be tabular. The samples from the Linglong granite were fresh. The quartz porphyry is a fine-grained grayish felsic rock that contains quartz and minor K-feldspar phenocrysts (Figures 2B, 3B). The volume fraction of the quartz phenocryst is <5%. The matrix contains micron-scale quartz and feldspar crystals. The K-feldspar in both phenocrysts and matrix was subjected to weathering and formed small amounts of sericite. The rhyolite porphyry sample (DZS-3) contained quartz and K-feldspar phenocrysts (Figures 2C, 3C). The phenocrysts were approximately 2–5 mm in diameter. The Dazeshan biotite granite (DZS-4) is a coarse-grained plutonic rock that intruded into the Linglong granite (Figure 1). The Dazeshan biotite granite had the same mineral assemblages as the Linglong granite but with larger crystal sizes.

3.1 Major and trace element analyses

Major element data for whole-rock samples were obtained by X-ray fluorescence (XRF) spectrometry on fused glass discs using a PANalytical AXIOS Minerals instrument at the Institute of Geology and Geophysics, Chinese Academy of Sciences. Glass discs for WD-XRF analyses were prepared by fusing 0.5 g of the standard sample with 5.0 g of lithium tetraborate-metaborate mixture (2:1) using Pt-Au crucibles and moulds on fusion equipment with gas burners. Loss on ignition (LOI) was measured as the weight loss of the samples after 1 h of baking at a constant temperature of 1,000°C in a muffle furnace. The ferrous iron content was determined using the titration method described by Xue et al. (2017). Whole-rock trace element analyses were performed at the National Research Center of Geoanalysis, Chinese Academy of Geological Science by inductively coupled

plasma mass spectrometry (ICP-MS) on a TJA PQ-ExCell system. Standards GSR1 and GSR9 were used to monitor the analytical reproducibility. 2σ uncertainties are <5% for elements >10 ppm and <10% for elements <10 ppm.

3.2 Zircon U-Pb dating and trace elements

Zircons were separated using conventional heavy liquid and magnetic separation techniques. They were mounted in epoxy and polished to a surface. Transmitted, reflected light and cathodoluminescence (CL) images were captured to acquire information about the inner structure, surface characteristics, and CL textures of the zircons, respectively. Laser ablation-inductively coupled plasma-mass spectrometry (LA-ICPMS) zircon U-Pb analyses were performed on an Agilent 7900 ICP-MS instrument equipped with a 193 nm laser ablation system at the Institute of Geology, Chinese Academy of Geological Sciences. A laser spot size of 30 μm was used to ionize the samples. The laser was operated at an energy of 2 J/cm^2 and a repetition rate of 5 Hz.

3.3 Zircon Lu-Hf isotopes

In situ zircon Lu-Hf isotopic analyses were performed on a Neptune MC-ICPMS coupled with a 193 nm laser ablation system at the National Research Center for Geoanalysis. An ArF excimer laser ablation system was used for the laser ablation analysis. The analyses used a laser repetition rate of 10 Hz at 100 mJ. A spot size of ca. 40 μm was applied depending on the size of the zircon grains. The ionized samples were carried by Ar gas. The detailed analytical procedures are described in (Wu et al., 2006).

4 Analytical results

4.1 Whole-rock major and trace elements

Eleven sample powders from three intrusions (except for the Linglong granite) were analyzed. The whole-rock geochemical data are presented in Figures 4, 5, 6 and Table 1. Overall, the silica contents of the quartz porphyry, rhyolite porphyry, and Dazeshan biotite granite are high (74–77 wt.%). In the total alkali vs. silica diagram (Figure 4A), these samples plot in the granite field. They belong to the high-K calc-alkaline series in the plot of SiO$_2$ vs. K$_2$O diagram (Figure 4B). In the plots of SiO$_2$ vs. CaO, Al$_2$O$_3$, MgO, TFeO, TiO$_2$, and P$_2$O$_5$, the three types of magmatic rocks display distinct major element contents (Figure 5). CaO concentrations in the Dazeshan biotite granite are the highest among the samples, while the quartz porphyry and rhyolite porphyry have CaO contents around 0.4 wt.%. The

FIGURE 4
Total alkaline vs. SiO$_2$ **(A)** and SiO$_2$ vs. K$_2$O **(B)** diagrams (Peccerillo and Taylor, 1976; Le Bas et al., 1986).
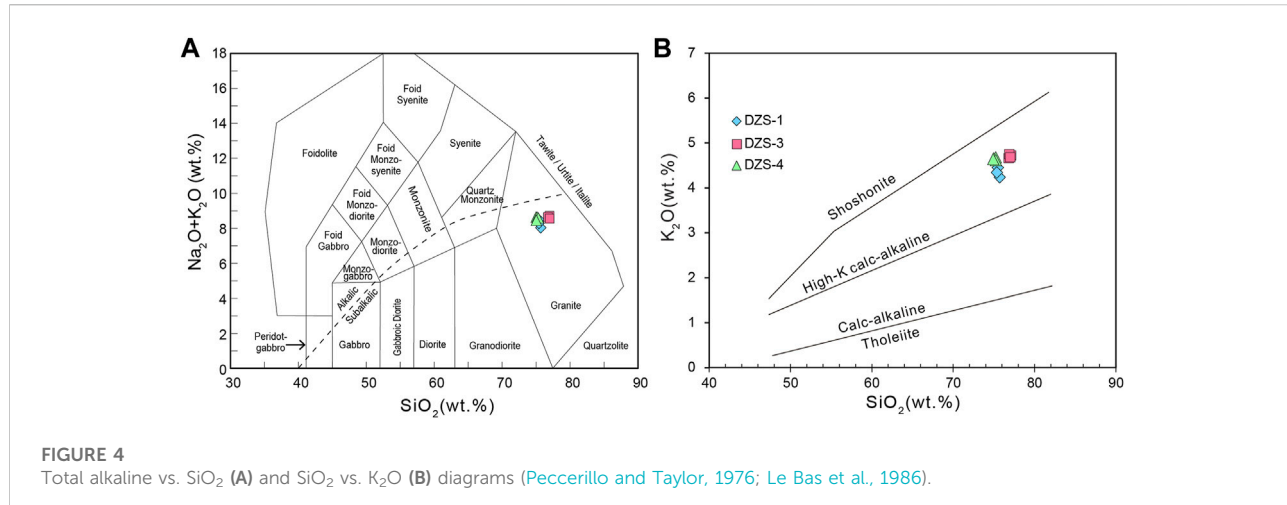
aluminum content for the quartz porphyry is the highest among the three intrusions (14.01–14.34 wt.%), about 1–2 wt.% higher than the other two suites. The Al$_2$O$_3$ contents in the Dazeshan biotite granite are in the range of 13.22–13.29 wt.%. The MgO concentrations in the intrusions are low (<0.4 wt.%) and show negative correlations with SiO$_2$ (Figure 5C). Total FeO contents are lower in the quartz porphyry and rhyolite porphyry (1.11–1.40 wt.% and 1.07–1.12 wt.%, respectively) and higher in the Dazeshan biotite granite (1.63–1.72 wt.%) (Figure 5D). The concentrations of TiO$_2$ and P$_2$O$_5$ are elevated in the Dazeshan biotite granite compared to those in the quartz and rhyolite porphyries (Figures 5E, F).

The whole-rock trace element data are normalized to the primitive mantle (PM) in REE and spider diagrams (Figure 6). In the REE diagram, the three intrusions display different enrichment and/or depletion patterns. The samples from quartz porphyry have low contents of total REE (20.7–27.7 ppm). Additionally, the light rare earth elements (La-Eu; LREE) are not strongly fractionated from the heavy rare earth elements (Gd-Lu; HREE) given the LREE/HREE ratios from 6.8 to 7.6. No apparent negative Eu anomaly is observed in the PM-normalized REE pattern. The calculated Eu/Eu* values range from 0.89 to 0.98 for the quartz porphyry samples (Eu/Eu* represents the europium anomaly calculated as Eu$_N$/(Sm$_N$×Gd$_N$)$^{0.5}$, the subscript "N" denotes the PM normalized value from McDonough and Sun, 1995). In the spider diagram (Figure 6B), high field strength elements (HFSE) like P and Ti in the quartz porphyry show negative anomalies. However, the large ion lithophile elements (LILE) like Rb and Ba, along with fluid mobile element Pb, are strongly enriched.

The REE patterns for the rhyolite porphyry and Dazeshan biotite granite show contrasting features compared to the quartz porphyry. Generally, these two intrusions have elevated REE concentrations compared to the quartz porphyry and display

listric-shaped patterns. Y These two porphyries also show obvious negative Eu anomalies. The Eu/Eu* for the rhyolite porphyry and Dazeshan biotite granite are 0.40–0.48 and 0.52–0.66, respectively. The LREE and HREE are strongly fractionated in these two intrusions. The LREE/HREE ratios are 23.7–26.0 for the rhyolite porphyry and 16.8–26.8 for the Dazeshan biotite granite. However, the Dazeshan biotite granite has higher total REE concentrations than that of the rhyolite porphyry (97.6–150.2 ppm vs. 69.7–96.4 ppm). In the spider diagram, the rhyolite porphyry and Dazeshan biotite granite display overall similar patterns except for Ba and Sr. The rhyolite porphyry shows more depletion of these two elements compared to the Dazeshan biotite granite (Figure 6B). Elements from Th to Pb in Figure 6B are elevated compared to the quartz porphyry.

4.2 Zircon U-Pb ages and trace elements

Four sets of zircon U-Pb ages and trace element data were obtained in this study. The analytical results are presented in Figures 7, 8 and Table 2 and Table 3. The LA-ICPMS zircon data from each rock type are briefly described below.

4.2.1 Quartz porphyry (DZS-1A)
Zircons from this sample are clear by microscopy and contain little mineral inclusions. Additionally, they display oscillatory zoning patterns under CL images. The lengths of these zircons are about 100–200 μm, while the widths are about 40–100 μm. Most of the zircons have a CL brighter grayish core without oscillatory zoning but are overgrown by CL dark rims with oscillatory zonings (Figure 7A). The zircon U-Pb ages in these two different areas are consistent. Twenty-one spot analyses on zircons were conducted. These isotope data cannot construct a well-defined Concordia U-Pb age but give a weighted mean ^{206}Pb-^{238}U age of 119.2 ± 1.0 Ma (Figures 7A, B;
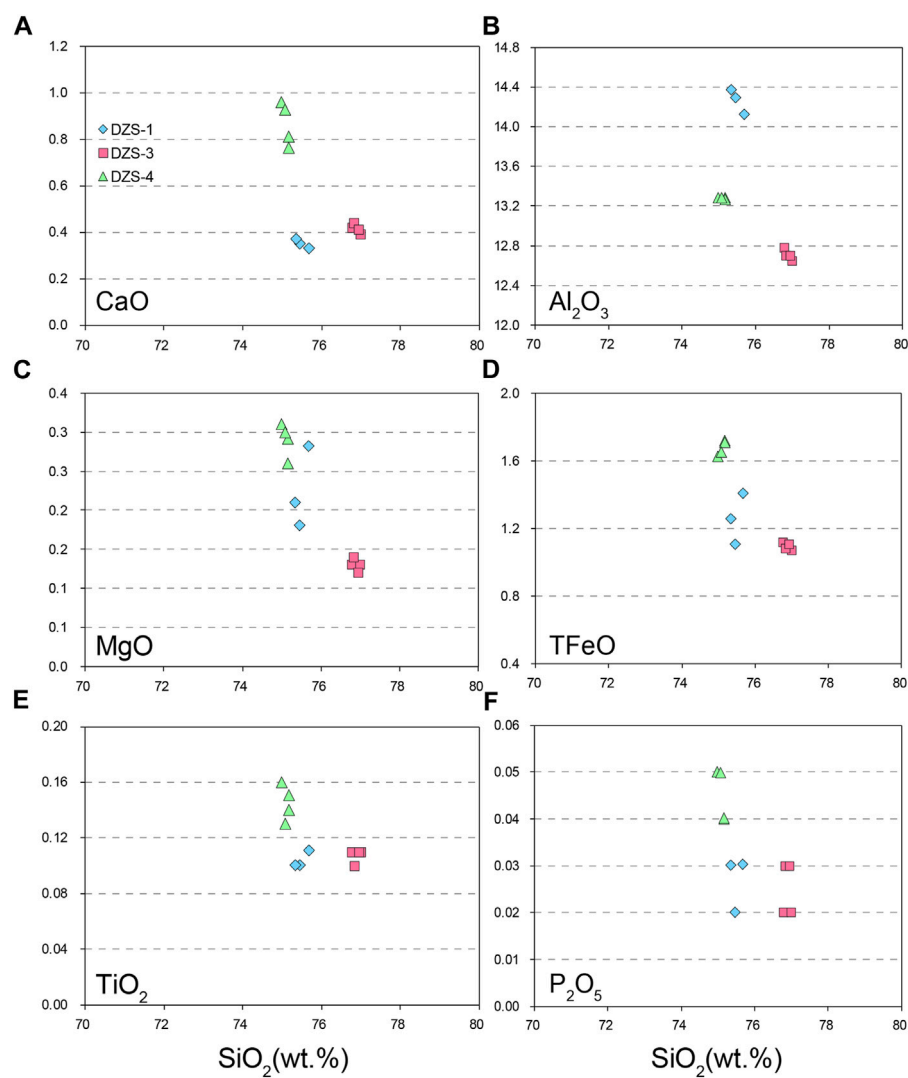
FIGURE 5
(A–F) Harker-type diagrams of whole-rock CaO, Al$_2$O$_3$, MgO, total FeO, TiO$_2$, and P$_2$O$_5$ versus SiO$_2$ contents for the studied intrusions.

MSWD = 3.6, N = 21). The U and Th concentrations in the zircons have wide ranges (201–3,411 ppm and 74–2084 ppm, respectively), whereas the Th/U ratios are relatively restricted between 0.36 and 1.03, with an average value of 0.62 (Table 2).

4.2.2 Linglong granite (DZS-2A)

Twenty-three zircons were analyzed in this sample. Most of these zircons are columnar with lengths of about 100–200 μm, and widths of 50–100 μm (mostly ~50 μm). Mineral inclusions like apatite or rutile are common in these zircons. The zircons have simple CL textures, with or without an oscillatory zoning rim. The cores of the zircons appear to be dark gray. Inherit zircons, however, are frequently observed and featured by bright CL (Figure 7C inset). Six of the twenty-four zircons underwent Pb loss and fall out of the Concordia line, yet they construct two

ages intercepting at 139 ± 37 and 1973 ± 48 Ma (MSWD = 4.9, N = 23). The two oldest zircons have ^{207}Pb-^{236}Pb ages of 2078 ± 30 Ma and 1838 ± 86 Ma, respectively. The young group of zircons constructs a weighted mean ^{206}Pb-^{238}Pb age of 140.2 ± 1.0 Ma (Figure 7D, MSWD = 2.4, N = 16). For the younger group zircons, which are considered the crystallization phase from the magma (see later discussion), the U concentrations range from 348 to 3,048 ppm, while the Th content varies between 58 and 1866 ppm (Table 2). The corresponding Th/U ratios are 0.08–1.29, with an average value of 0.47.

4.2.3 Rhyolite porphyry (DZS-3A)

Twenty-four zircons were separated from the rhyolite porphyry sample. Zircon morphology exhibits tiny differences from the quartz porphyry and Linglong granite samples. These
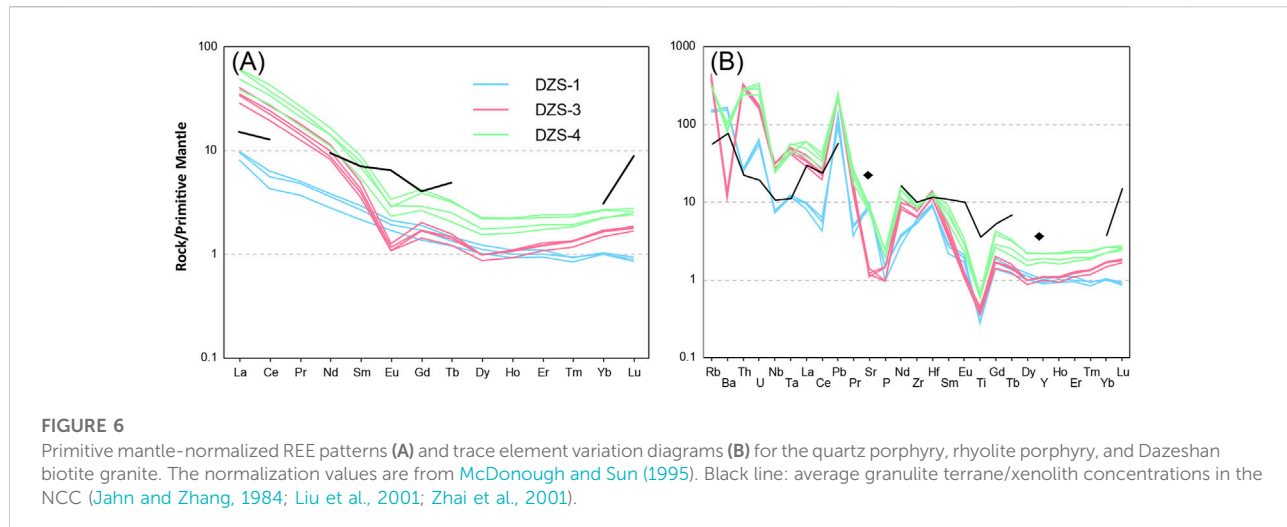
FIGURE 6
Primitive mantle-normalized REE patterns **(A)** and trace element variation diagrams **(B)** for the quartz porphyry, rhyolite porphyry, and Dazeshan biotite granite. The normalization values are from McDonough and Sun (1995). Black line: average granulite terrane/xenolith concentrations in the NCC (Jahn and Zhang, 1984; Liu et al., 2001; Zhai et al., 2001).

grains are equally sized, with length-to-width ratios of around 1.5–2.0. The lengths of most zircons are around 150 μm. Their CL characters vary. Some zircons have a bright core with CL dark/bright oscillatory zoning rims, while others have CL bright oscillatory zoning in the whole grain. Nevertheless, the zircon ages in these different areas are the same. All the zircons construct a Concordia U-Pb age of 120.7 ± 0.5 Ma (Figure 7E; MSWD = 1.7, N = 24 and a weighted mean ^{206}Pb-^{238}Pb age of 120.6 ± 0.5 Ma (Figure 7F; MSWD = 1.5, N = 24). The zircon U and Th concentrations are 179–1,533 ppm and 191–1,037 ppm, respectively. The average U and Th concentrations are 575 ppm and 360 ppm, respectively. The zircon Th/U ratios are 0.42–1.58.

4.2.4 Dazeshan biotite granite (DZS-4A)

Zircons from the biotite granite are characterized by low length-to-width ratios (1–1.5). Most of these zircons are 100–150 μm in size and have CL bright/dark oscillatory zoning occupying the whole zircon grain. Generally, the CL bright zone is rimmed by a CL dark zone with or without oscillatory zoning patterns. The data of the 26 analyzed zircons yielded ages that intercept at 1,364 ± 800 Ma and 118.5 ± 2.0 Ma (Figure 7G, MSWD = 0.81). The weighted mean ^{206}Pb-^{238}Pb age is 119.9 ± 0.7 Ma (Figure 7H, MSWD = 1.9). The zircon U concentrations are 181–3,275 ppm, while the Th concentrations are 148–2,233 ppm. The Th/U ratios in zircons range from 0.47 to 1.46 (Table 2).

Zircon trace element data of the four samples are presented in Figure 8 and Table 3. All zircons feature HREE enrichment but LREE depletion (except for Ce, which displays a strong positive anomaly) in PM-normalized REE patterns (Figures 8A–D). Europium shows a relatively weak negative anomaly in zircons from the quartz porphyry. However, the negative Eu anomalies are strikingly obvious in the other three zircon samples.

4.3 Zircon Lu-Hf isotopes

Zircon Hf isotopes were analyzed in rhyolite porphyry and the Dazeshan biotite granite. The hafnium isotope data are presented in Figure 9 and Table 4. For the rhyolite porphyry, ^{176}Hf/^{177}Hf values are 0.282133–0.282181. The calculated $\varepsilon_{Hf}(t)$ was −18.3 to −20.0. The two stage model ages are 3.2 to 3.4 Ga. Five spot analyses of zircons from the Dazeshan biotite granite give a ^{176}Hf/^{177}Hf values between 0.282130 and 0.282195 ($\varepsilon_{Hf}(t)$ = −17.8 to −20.2).

5 Discussion

5.1 Genesis of the ~120 Ma magmatic rocks

Granites are produced predominantly by anatexis of crustal rocks (Brown, 2013; Clemens et al., 2020), although in some cases, the granites are generated by fractional crystallization of mantle-derived melts (Soesoo, 2000; Thompson et al., 2002). For the samples investigated in this study, the SiO$_2$ contents of the three intrusions (except for the Linglong granite) are very high (74–77 wt. %). Meanwhile, no considerable mafic melts occurred along with these granites (Figure 1), eliminating the possibility of fractional crystallization of mantle-derived melts. The Hf isotope compositions from the zircons also provide information on the sources of the melts well (Figure 9). The $\varepsilon_{Hf}(t)$ values are restricted for both the rhyolite porphyry and Dazeshan biotite granite (ca. −18 to −20), comparable to other granitic rocks reported in the Jiaodong Penisula (e.g., Linglong granite and Aishan granodiorite). For example, the Linglong granite was interpreted to be the melting products of the Archean lower crust, with almost no contribution from the mantle (Ma et al.,

TABLE 1 Major (*wt* %) and trace (*ppm*) element concentrations for igneous rocks in the Dazeshan region.

	DZS-1A	DZS-1B	DZS-1E	DZS-3A	DZS-3B	DZS-3D	DZS-3E	DZS-4A	DZS-4B	DZS-4D	DZS-4E
SiO_2	75.23	75.06	75.18	76.83	77.04	76.75	77.02	74.96	75.04	74.89	75.11
Al_2O_3	14.25	14.01	14.34	12.79	12.65	12.69	12.71	13.28	13.26	13.22	13.29
TFe_2O_3	1.11	1.40	1.26	1.12	1.07	1.08	1.11	1.63	1.72	1.71	1.66
MgO	0.18	0.28	0.21	0.13	0.13	0.14	0.12	0.31	0.26	0.29	0.30
CaO	0.35	0.33	0.37	0.42	0.39	0.44	0.41	0.96	0.81	0.76	0.93
Na_2O	4.01	3.74	3.93	3.97	3.89	3.93	3.88	3.90	3.88	3.92	3.87
K_2O	4.44	4.21	4.35	4.67	4.74	4.72	4.70	4.67	4.64	4.62	4.65
TiO_2	0.10	0.11	0.10	0.11	0.11	0.10	0.11	0.16	0.14	0.15	0.13
P_2O_5	0.02	0.03	0.03	0.02	0.02	0.03	0.03	0.05	0.04	0.04	0.05
MnO	0.01	0.01	0.01	0.01	0.02	0.02	0.01	0.04	0.04	0.03	0.05
LOI	0.67	0.97	0.92	0.33	0.28	0.30	0.29	0.38	0.25	0.34	0.39
Total	100.36	100.14	100.70	100.41	100.35	100.20	100.39	100.34	100.08	99.97	100.43
Mg#	24	28	24	19	16	40	38	40	48	32	34
ppm											
P	88	132	131	87	87	131	131	218	175	175	218
Ti	342	344	334	428	541	460	507	779	695	713	796
Sc	1.68	1.70	1.62	1.57	1.53	1.38	1.29	2.16	2.08	2.39	2.41
V	3.68	3.11	3.99	2.25	2.89	3.36	2.79	6.88	6.41	6.48	7.03
Cr	3.63	7.78	8.75	5.70	17.6	8.57	7.70	6.60	5.58	8.37	7.96
Co	0.36	0.48	0.77	0.57	0.57	0.69	0.67	1.40	1.10	1.21	1.18
Ni	0.36	0.98	2.89	0.83	0.25	1.87	1.62	1.65	1.67	2.25	3.58
Rb	89.9	92.4	87.1	227	264	242	275	191	194	195	189
Sr	194	179	162	23	28	24	22	174	157	153	181
Zr	63.8	58.1	56.7	66.9	87.0	67.9	80.3	90.5	86.8	92.1	90.9
Nb	5.12	4.77	4.84	16.9	20.5	18.1	20.9	16.0	16.6	16.6	16.1
Ba	1,114	1,084	1,014	75.1	88.6	87.6	76.3	660	528	570	682
Y	3.86	4.37	3.97	4.24	4.66	4.74	4.70	8.11	9.36	7.31	9.32
La	5.27	6.32	6.24	18.7	22.9	21.9	26.4	38.6	31.4	25.0	39.1
Ce	7.17	10.6	9.27	32.4	40.5	37.3	45.1	62.8	56.7	46.9	72.3
Pr	0.94	1.29	1.24	3.26	3.99	3.69	4.66	6.10	5.42	4.40	6.81
Nd	3.52	4.77	4.47	10.2	12.3	11.0	14.3	17.9	17.9	13.8	20.9
Sm	0.88	1.19	1.09	1.43	1.73	1.60	2.02	2.81	3.17	2.21	3.63
Eu	0.26	0.33	0.30	0.17	0.18	0.17	0.20	0.45	0.44	0.36	0.52
Gd	0.75	1.03	0.93	0.78	0.92	0.91	1.09	1.58	2.11	1.43	2.30
Tb	0.12	0.15	0.13	0.12	0.15	0.14	0.16	0.25	0.32	0.20	0.33
Dy	0.69	0.83	0.76	0.59	0.67	0.66	0.66	1.19	1.52	1.04	1.48

TABLE 1 (*Continued*) Major (*wt %*) and trace (*ppm*) element concentrations for igneous rocks in the Dazeshan region.

	DZS-1A	DZS-1B	DZS-1E	DZS-3A	DZS-3B	DZS-3D	DZS-3E	DZS-4A	DZS-4B	DZS-4D	DZS-4E
Ho	0.14	0.16	0.15	0.14	0.16	0.16	0.16	0.27	0.33	0.24	0.33
Er	0.42	0.48	0.44	0.48	0.56	0.53	0.54	0.85	1.05	0.76	0.98
Tm	0.06	0.06	0.06	0.08	0.09	0.09	0.09	0.13	0.16	0.13	0.16
Yb	0.44	0.46	0.44	0.65	0.76	0.73	0.73	0.99	1.18	0.98	1.16
Lu	0.06	0.06	0.06	0.11	0.12	0.12	0.13	0.16	0.19	0.17	0.17
Hf	2.67	2.61	2.49	3.20	3.95	3.31	3.83	3.46	3.54	3.73	3.72
Ta	0.44	0.46	0.42	1.56	1.82	1.62	1.87	1.53	2.08	1.67	1.99
Pb	20.2	14.2	14.7	33.7	36.8	33.9	36.9	35.6	36.9	33.9	36.6
Th	1.97	2.10	2.02	23.5	26.7	25.7	25.9	22.2	20.9	23.0	19.5
U	1.11	1.30	1.27	3.27	3.63	3.32	3.45	5.81	6.42	6.88	4.89
Cs	0.81	0.80	0.85	1.76	1.96	1.92	2.14	3.82	5.89	3.79	6.38
Cu	3.28	4.29	6.01	5.72	2.90	5.06	4.71	3.83	3.76	5.39	5.06
Zn	6.28	4.47	5.58	1.37	1.62	1.52	1.98	12.9	13.4	11.6	14.3
Ga	16.3	17.4	17.0	14.3	17.3	15.5	17.7	17.1	17.1	15.2	18.1
Bi	0.05	0.09	0.09	0.03	0.02	0.02	0.03	0.12	0.19	0.11	0.22

2013; Li et al., 2019). The two stage model ages calculated *via* zircon Hf isotope compositions are 3.2–3.4 Ga for the rhyolite porphyry and Dazeshan biotite granite (Table 4), demonstrating their ancient continental crust source. Therefore, these granite rocks are generated by crustal anatexis.

From the perspective of the whole-rock and zircon trace element data, the three intrusions have strikingly different geochemical features (Figures 6, 10). This implies that these intrusions probably experienced distinct melting or differentiation processes. The following section discusses the chemical variations in these magmatic rocks and their magmatic evolution.

5.1.1 Quartz porphyry (DZS-1)

The quartz porphyry is characterized by low LREE content and a lack of negative Eu anomaly in the REE pattern (Figure 6A). The LREE concentrations in the quartz porphyry here are even lower than the average concentrations of the granulite terranes/xenoliths in the NCC, which were regarded as representative of the lower crust fragments (Liu et al., 1999; Zhai et al., 2001; Liu et al., 2004). Partial melting of the granulite rocks would give rise to higher REE content in the melt considering their incompatibility. The discordant REE patterns between the quartz porphyry and granulite terranes/xenoliths differ from what would be expected if the quartz porphyry is the melting product of lower-crust granulite. Magmatic processes

like fractionation crystallization or magma mixing could exert a conspicuous influence on the compositions of the melt (DePaolo, 1981; Yang et al., 2004; Cao et al., 2022).

The whole-rock major and trace elements, trace elements ratios (Th/Nb, La/Sm, and Rb/Sr), and Mg# values vary little among the three samples from the quartz porphyry, indicating that fractionation crystallization of major mineral phases (e.g., amphibole, K-feldspar) probably plays a negligible role in generating such low REE concentrations. This supposition is supported by the fact that Dy/Yb in zircons does not decrease with increasing Hf concentrations (Figure 11A), implying no considerable amphibole fractionation (Davidson et al., 2007). Rather, Dy/Yb increases with Hf enrichment in zircons. This may indicate zircon separation, which reduces the Yb contents of the remnant melt. Eu/Eu* values in zircon are high and are not linearly correlated with Hf concentrations (Figure 11B), eliminating the potential influence of plagioclase fractionation.

The effects of magma mixing, if it occurs, rely on the composition of the mixing end-members. The relatively depleted features of LREE require at least one end-member of REE-depleted melt, most likely the depleted mantle source. However, the low Mg# numbers (<30), together with low Ni and Co concentrations (<2 ppm) imply that the mantle component is not involved in the magma genesis for the quartz porphyry. Therefore, the quartz porphyry was probably generated by the remelting of the REE-depleted lower crust at around 120 Ma.
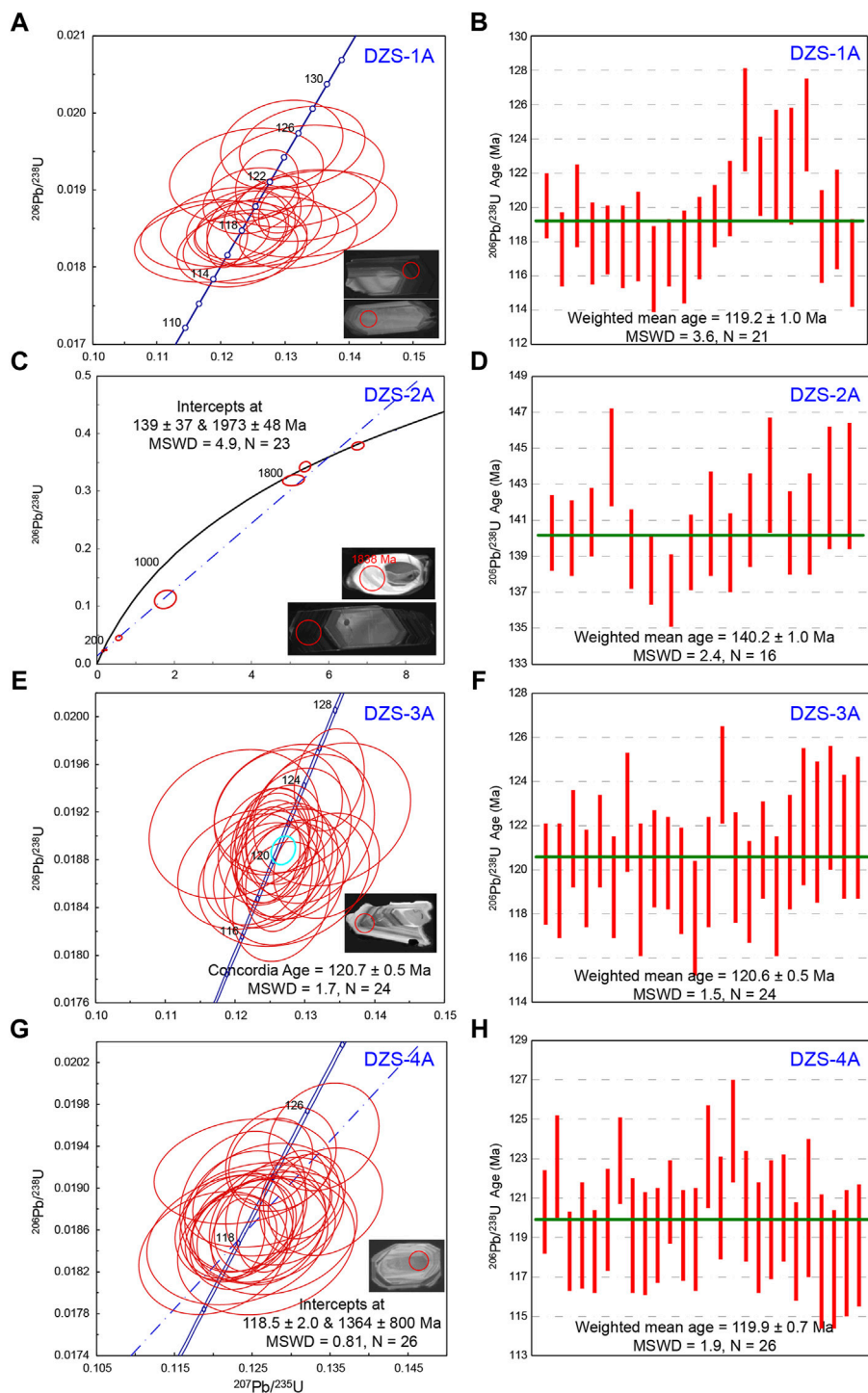
FIGURE 7
Zircon U-Pb concordia and weighted mean ^{238}U/^{206}Pb ages of the studied magmatic rocks. The red circles in the zircon grains are analytical spots and are 30 μm in diameter. **(A,B)** Quartz porphyry; **(C,D)** Linglong granite; **(E,F)** rhyolite porphyry; **(G,H)** Dazeshan biotite granite.

5.1.2 Rhyolite porphyry (DZS-3)

The rhyolite porphyry also features extremely low Mg$^{#}$ values and low Ni and Co concentrations (Figure 10A; Table 1), ruling out the possibility of the involvement of the mantle component. These rocks show obvious Sr, P, and Ti depletion. Moreover, they are characterized by
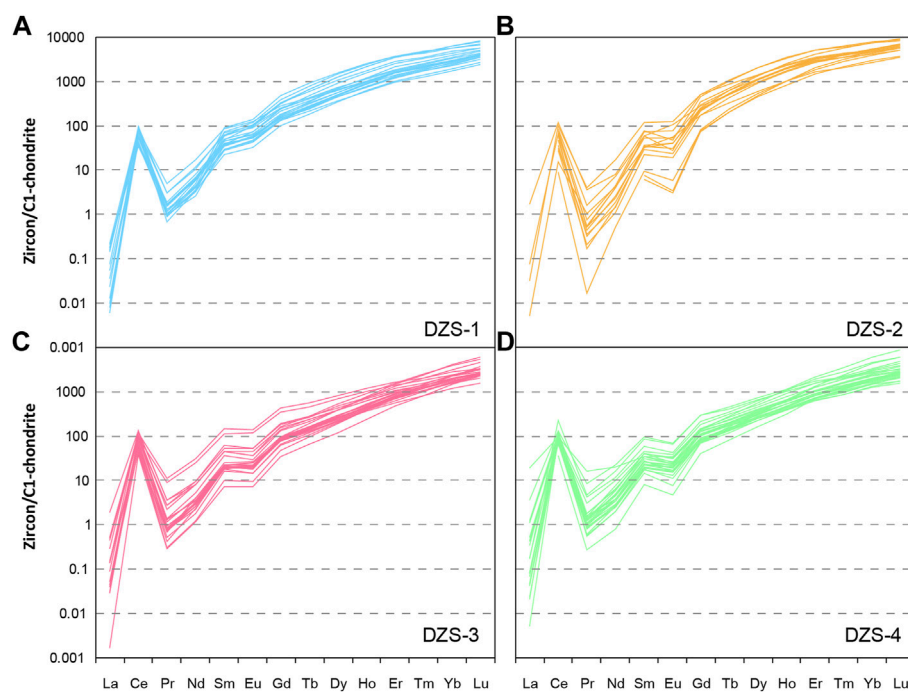
FIGURE 8
Zircon REE concentrations of quartz porphyry, Linglong granite, rhyolite porphyry, and Dazeshan biotite granite, respectively **(A–D)**. The normalization values are from Sun and McDonough (1989).

negative Eu anomalies and listric-shaped REE patterns (Figure 6A). These geochemical features imply that fractionation crystallization plays an important role in generating rhyolite porphyry. As shown in Figure 10B, whole-rock Dy/Yb ratios remain consistent with increasing Rb/Sr ratios, although the Rb/Sr ratios only show slight variation within samples. Zircon trace elements likely reflect more clear trends. The Zircon Dy/Yb ratio decreases from 0.45 to 0.1 when the Hf concentrations in zircon increase from 7,000 to 15,000 ppm (Figure 11A). Eu/Eu* values in zircon also show a decreasing trend with increasing Hf content (Figure 11B). This evidence supports the fractionation crystallization of amphibole and plagioclase. The amphibole incorporates more MREE (e.g., Dy) compared to HREE (e.g., Yb), thus leading to higher Dy/Yb values in the remnant melt (Davidson et al., 2007). Hafnium is an incompatible element during magmatic differentiation and its concentration will increase in the melt with progressive crystallization (Rollinson, 1993), which can be recorded in the co-crystallized zircon. In the current case, Dy/Yb decreases with increasing Hf content in zircon, implying amphibole fractionation. The negative Eu anomaly and decreasing zircon Eu/Eu* trend along with rising Hf concentrations reflect plagioclase fractionation because Eu preferentially partitions into plagioclase and replaces Ca in the lattice site under most geological environments.

Negative zircon Hf isotopes (−18.3 to −20.0) and the Archean two-stage Hf model ages suggest that the rhyolite porphyry is derived from the old crust source, consistent with the ancient nature of the NCC (Liu et al., 1992). Therefore, the rhyolite porphyry was derived from the melting of the ancient lower crust and experienced amphibole and plagioclase fractionation during magmatic evolution.

5.1.3 Dazeshan biotite granite (DZS-4)

The Dazeshan biotite granite shares overall similar geochemical features to those of the rhyolite porphyry in both REE pattern and spider diagram (Figure 6). Zircon trace elements and Hf isotopic compositions were almost identical (Figures 8–9, 11). Therefore, the origin of Dazeshan biotite granite was certainly the same as that of the rhyolite porphyry (crust anatexis with limited mantle contribution). The minor differences in REE and Sr concentrations were likely the result of discrepancies in differentiation processes between these two intrusions. As noted above, the negative Eu anomaly in the PM-normalized REE pattern and low zircon Eu/Eu* values indicated plagioclase fractionation. The listric-shaped REE pattern and decreasing zircon Dy/Yb values with rising Hf concentrations reflect amphibole-dominated fractionation. Therefore, it is reasonable to conclude that the Dazeshan biotite granite is derived from the partial

TABLE 2 LA-ICPMS U-Pb age data for zircons from Dazeshan magmatic rocks.

No.	207 Pb/235U	±σ %	206 Pb/238U	±σ %	ρ	207Pb/206 Pb	±σ %	207Pb/206 Pb age (Ma)	±σ	206 Pb/238U age (Ma)	±σ	207 Pb/235U age (Ma)	±σ	U (ppm)	Th (ppm)	Th/U
DZS-1A																
1	0.1297	0.0039	0.0188	0.0003	0.1710	0.0494	0.0015	150	65	120.1	1.9	123.5	3.5	1,307	758	0.58
2	0.1321	0.0075	0.0184	0.0003	0.0470	0.0518	0.0030	180	110	117.5	2.1	125.0	6.7	316	211	0.67
3	0.1332	0.0090	0.0188	0.0004	0.0568	0.0514	0.0035	140	130	120.1	2.4	125.7	8.0	230	237	1.03
4	0.1271	0.0092	0.0185	0.0004	0.1030	0.0502	0.0037	110	140	117.9	2.4	120.2	8.3	196	144	0.74
5	0.1231	0.0058	0.0185	0.0003	0.1388	0.0485	0.0024	77	97	118.1	2.0	117.3	5.2	515	358	0.70
6	0.1175	0.0082	0.0184	0.0004	0.0592	0.0461	0.0034	−30	130	117.7	2.4	112.7	7.6	259	209	0.81
7	0.1252	0.0086	0.0185	0.0004	−0.0354	0.0494	0.0036	70	140	118.3	2.6	118.6	7.8	180	91	0.51
8	0.1226	0.0077	0.0182	0.0004	0.1759	0.0482	0.0030	70	120	116.4	2.5	116.6	7.0	267	127	0.47
9	0.1210	0.0026	0.0184	0.0003	0.3541	0.0475	0.0010	75	46	117.3	1.9	115.8	2.4	3,411	2084	0.61
10	0.1200	0.0110	0.0183	0.0004	0.1542	0.0476	0.0044	10	170	117.1	2.7	114.0	10.0	184	115	0.62
11	0.1242	0.0052	0.0185	0.0004	0.3177	0.0487	0.0020	117	86	118.2	2.4	118.6	4.7	1,119	471	0.42
12	0.1292	0.0027	0.0187	0.0003	0.2960	0.0494	0.0011	154	46	119.5	1.8	123.2	2.4	2,601	1,356	0.52
13	0.1247	0.0061	0.0189	0.0004	0.0785	0.0481	0.0025	56	98	120.5	2.2	118.7	5.5	466	211	0.45
14	0.1295	0.0078	0.0196	0.0005	0.1936	0.0481	0.0029	60	120	125.1	3.0	123.7	7.2	270	135	0.50
15	0.1272	0.0040	0.0191	0.0004	0.2233	0.0484	0.0016	97	68	121.8	2.3	121.8	3.7	1,206	862	0.71
16	0.1240	0.0098	0.0192	0.0005	−0.0522	0.0473	0.0039	−30	150	122.5	3.2	117.4	8.8	201	200	0.99
17	0.1320	0.0110	0.0192	0.0005	0.0577	0.0507	0.0047	100	180	122.4	3.4	126.0	11.0	196	118	0.60
18	0.1327	0.0080	0.0196	0.0004	0.2092	0.0491	0.0029	90	110	124.8	2.7	125.5	7.2	262	95	0.36
19	0.1211	0.0086	0.0185	0.0004	0.2171	0.0474	0.0034	10	130	118.3	2.7	114.8	7.7	190	110	0.58
20	0.1340	0.0110	0.0187	0.0005	0.1470	0.0522	0.0042	130	150	119.3	2.9	125.9	9.6	169	74	0.43
21	0.1238	0.0079	0.0183	0.0004	0.1023	0.0486	0.0031	70	130	116.7	2.5	117.5	7.1	258	212	0.82
DZS-2A																
1	0.1492	0.0036	0.0220	0.0003	0.2866	0.0490	0.0011	134	51	141.0	3.2	140.3	2.1	1844	937	0.51

TABLE 2 (*Continued*) LA-ICPMS U-Pb age data for zircons from Dazeshan magmatic rocks.

No.	207 Pb/235U	±σ %	206 Pb/238U	±σ %	ρ	207Pb/206 Pb	±σ %	207Pb/206 Pb age (Ma)	±σ	206 Pb/238U age (Ma)	±σ	207 Pb/235U age (Ma)	±σ	U (ppm)	Th (ppm)	Th/U
2	0.1460	0.0036	0.0220	0.0003	0.3123	0.0479	0.0012	81	51	138.2	3.2	140.0	2.1	1835	1,188	0.65
3	0.1536	0.0039	0.0221	0.0003	0.2095	0.0503	0.0013	187	55	144.9	3.4	140.9	1.9	1,572	683	0.43
4	0.1536	0.0052	0.0227	0.0004	0.3013	0.0497	0.0017	157	74	144.8	4.6	144.5	2.7	1,467	789	0.54
5	0.1475	0.0028	0.0219	0.0004	0.2327	0.0489	0.0010	135	45	139.6	2.5	139.4	2.2	3,048	1866	0.61
6	0.1455	0.0033	0.0217	0.0003	0.1645	0.0485	0.0012	111	53	137.7	3.0	138.2	1.9	1,530	1,106	0.72
7	0.1465	0.0055	0.0215	0.0003	0.1122	0.0492	0.0018	137	80	138.8	4.9	137.1	2.0	593	188	0.32
8	0.1521	0.0061	0.0218	0.0003	0.0626	0.0508	0.0021	192	85	143.9	5.5	139.2	2.1	632	172	0.27
9	0.1454	0.0097	0.0221	0.0005	-0.0327	0.0478	0.0032	50	130	136.5	8.6	140.8	2.9	217	87	0.40
10	0.1536	0.0050	0.0218	0.0004	0.2430	0.0508	0.0016	209	68	144.8	4.4	139.2	2.2	852	258	0.30
11	0.1573	0.0056	0.0221	0.0004	0.2835	0.0514	0.0018	218	75	147.9	4.9	141.0	2.6	662	202	0.30
12	0.1508	0.0071	0.0225	0.0005	0.3310	0.0485	0.0022	100	93	141.9	6.3	143.5	3.2	453	58	0.13
13	0.1478	0.0043	0.0220	0.0004	0.2735	0.0484	0.0014	104	61	139.7	3.8	140.3	2.3	1,444	1,360	0.94
14	0.1540	0.0057	0.0221	0.0004	0.3470	0.0500	0.0017	167	72	145.0	5.0	140.8	2.8	849	72	0.08
15	0.1463	0.0077	0.0224	0.0005	0.3108	0.0469	0.0024	7	97	137.7	6.8	142.8	3.4	348	450	1.29
16	0.1553	0.0076	0.0224	0.0006	0.2971	0.0500	0.0024	180	100	146.2	6.6	142.9	3.5	876	68	0.08
17	6.7600	0.1300	0.3787	0.0056	0.4781	0.1295	0.0023	2078	30	2080	17.0	2069	26.0	134	85	0.63
18	5.0900	0.2300	0.3190	0.0077	0.2145	0.1181	0.0056	1838	86	1814	38.0	1781	37.0	14	40	2.85
19	5.3900	0.1200	0.3425	0.0072	0.5861	0.1123	0.0021	1826	35	1878	19.0	1900	35.0	164	96	0.59
20	0.1716	0.0078	0.0226	0.0005	0.3789	0.0546	0.0023	345	90	160.2	6.7	143.8	2.8	869	244	0.28
21	1.7700	0.2300	0.1120	0.0130	0.9813	0.1054	0.0034	1,687	63	921.0	78.0	668.0	71.0	349	86	0.25
22	0.2270	0.0170	0.0241	0.0006	0.3051	0.0678	0.0047	710	130	206.0	14.0	153.2	3.5	418	150	0.36
23	0.5630	0.0680	0.0451	0.0035	0.9629	0.0813	0.0036	1,144	89	423.0	38.0	283.0	21.0	480	160	0.33
DZS-3A																
1	0.1331	0.0062	0.0188	0.0004	0.0072	0.0508	0.0025	180	100	126.3	5.6	119.8	2.3	360	187	0.52
2	0.1223	0.0086	0.0187	0.0004	0.0557	0.0472	0.0035	-10	130	116.1	7.7	119.5	2.6	236	224	0.95

TABLE 2 (*Continued*) LA-ICPMS U-Pb age data for zircons from Dazeshan magmatic rocks.

No.	207 Pb/235U	±σ %	206 Pb/238U	±σ %	ρ	207Pb/206 Pb	±σ %	207Pb/206 Pb age (Ma)	±σ	206 Pb/238U age (Ma)	±σ	207 Pb/235U age (Ma)	±σ	U (ppm)	Th (ppm)	Th/U
3	0.1270	0.0045	0.0190	0.0003	0.2608	0.0480	0.0017	81	73	121.1	4.1	121.4	2.2	885	337	0.38
4	0.1287	0.0063	0.0187	0.0003	0.2528	0.0493	0.0024	121	98	122.3	5.6	119.6	2.2	374	255	0.68
5	0.1254	0.0044	0.0190	0.0003	0.1855	0.0473	0.0016	56	72	119.7	4.0	121.3	2.1	1,101	463	0.42
6	0.1245	0.0062	0.0187	0.0004	0.0921	0.0480	0.0024	60	100	118.5	5.6	119.2	2.3	375	228	0.61
7	0.1262	0.0075	0.0192	0.0004	0.0237	0.0479	0.0030	30	120	119.7	6.8	122.6	2.7	260	237	0.91
8	0.1270	0.0100	0.0187	0.0005	-0.0235	0.0492	0.0040	60	150	120.2	8.9	119.1	3.0	179	283	1.58
9	0.1251	0.0045	0.0189	0.0004	0.2859	0.0479	0.0017	91	72	119.4	4.1	120.5	2.2	998	691	0.69
10	0.1247	0.0038	0.0188	0.0003	0.3156	0.0482	0.0015	89	64	119.1	3.4	120.3	2.1	1,278	1,037	0.81
11	0.1228	0.0060	0.0187	0.0004	0.2471	0.0479	0.0023	68	97	117.1	5.4	119.5	2.4	483	261	0.54
12	0.1266	0.0057	0.0185	0.0004	0.0700	0.0497	0.0025	130	100	121.3	5.0	117.8	2.6	512	241	0.47
13	0.1275	0.0059	0.0188	0.0004	0.1818	0.0499	0.0024	136	98	121.9	5.4	119.9	2.5	435	353	0.81
14	0.1335	0.0041	0.0195	0.0004	0.3119	0.0500	0.0015	170	63	126.9	3.7	124.3	2.2	1,533	921	0.60
15	0.1270	0.0057	0.0188	0.0004	0.1453	0.0497	0.0024	128	96	120.9	5.2	120.1	2.5	492	234	0.48
16	0.1263	0.0039	0.0186	0.0004	0.2897	0.0496	0.0016	153	65	120.6	3.5	119.0	2.3	1,235	523	0.42
17	0.1250	0.0046	0.0189	0.0004	0.1310	0.0484	0.0019	94	78	119.2	4.1	120.9	2.2	799	409	0.51
18	0.1270	0.0070	0.0186	0.0004	0.1238	0.0498	0.0028	130	110	120.7	6.3	118.8	2.7	348	189	0.54
19	0.1247	0.0058	0.0189	0.0004	0.0851	0.0484	0.0024	87	98	119.5	5.4	120.8	2.6	544	290	0.53
20	0.1339	0.0092	0.0192	0.0005	0.0650	0.0517	0.0037	160	140	127.4	8.4	122.4	3.1	211	251	1.19
21	0.1308	0.0075	0.0191	0.0005	0.0510	0.0504	0.0030	150	120	124.1	6.7	121.7	3.2	281	279	0.99
22	0.1278	0.0088	0.0192	0.0004	0.1647	0.0490	0.0034	70	130	120.9	7.9	122.8	2.8	265	191	0.72
23	0.1288	0.0064	0.0190	0.0004	0.1900	0.0496	0.0024	135	99	122.4	5.8	121.5	2.8	442	239	0.54
24	0.1198	0.0099	0.0191	0.0005	0.1635	0.0461	0.0038	−70	150	113.3	8.9	121.9	3.2	185	305	1.65
DZS-4A																
1	0.1257	0.0078	0.0188	0.0003	0.0917	0.0490	0.0031	70	120	119.3	7.0	120.3	2.1	284	203	0.72
2	0.1238	0.0093	0.0192	0.0004	0.1395	0.0472	0.0035	−20	140	117.9	8.4	122.6	2.6	208	235	1.13

TABLE 2 (*Continued*) LA-ICPMS U-Pb age data for zircons from Dazeshan magmatic rocks.

No.	207 Pb/235U	±σ %	206 Pb/238U	±σ %	ρ	207Pb/206 Pb	±σ %	207Pb/206 Pb age (Ma)	±σ	206 Pb/238U age (Ma)	±σ	207 Pb/235U age (Ma)	±σ	U (ppm)	Th (ppm)	Th/U
3	0.1232	0.0028	0.0185	0.0003	0.4343	0.0484	0.0010	121	47	117.8	2.5	118.3	2.0	3,275	2,233	0.68
4	0.1226	0.0056	0.0187	0.0004	0.1726	0.0485	0.0024	77	96	116.9	5.0	119.1	2.7	403	390	0.97
5	0.1223	0.0048	0.0185	0.0003	0.3027	0.0483	0.0017	99	74	117.3	4.3	118.3	2.1	1,021	539	0.53
6	0.1292	0.0062	0.0188	0.0004	0.1193	0.0497	0.0024	150	99	122.7	5.6	119.9	2.6	540	787	1.46
7	0.1274	0.0044	0.0193	0.0003	0.2315	0.0483	0.0016	94	69	121.5	3.9	122.9	2.2	1,215	715	0.59
8	0.1270	0.0061	0.0187	0.0005	0.1663	0.0496	0.0025	150	100	121.0	5.5	119.1	2.9	707	676	0.96
9	0.1264	0.0076	0.0186	0.0004	0.0393	0.0501	0.0032	110	120	120.0	6.8	118.7	2.6	353	271	0.77
10	0.1273	0.0035	0.0187	0.0004	0.4760	0.0497	0.0012	167	53	121.4	3.1	119.1	2.4	2,703	1,268	0.47
11	0.1317	0.0043	0.0189	0.0003	0.2500	0.0509	0.0017	204	71	125.4	3.9	120.8	2.1	1,351	1,032	0.76
12	0.1254	0.0043	0.0186	0.0004	0.2975	0.0488	0.0016	118	71	119.7	3.9	119.1	2.3	1,159	679	0.59
13	0.1227	0.0062	0.0186	0.0004	0.1707	0.0478	0.0023	80	100	117.0	5.5	118.9	2.6	550	406	0.74
14	0.1287	0.0058	0.0193	0.0004	0.3724	0.0487	0.0020	111	83	122.5	5.2	123.1	2.6	940	790	0.84
15	0.1305	0.0037	0.0189	0.0004	0.4446	0.0500	0.0013	184	57	124.3	3.3	120.5	2.6	1825	1,428	0.78
16	0.1342	0.0058	0.0195	0.0004	0.1741	0.0507	0.0022	186	92	128.7	5.5	124.4	2.6	626	561	0.90
17	0.1268	0.0077	0.0189	0.0004	0.2470	0.0494	0.0030	90	120	121.1	7.1	120.6	2.8	298	230	0.77
18	0.1259	0.0070	0.0186	0.0004	0.1977	0.0496	0.0028	110	110	120.4	6.4	119.0	2.8	315	214	0.68
19	0.1242	0.0064	0.0188	0.0005	0.1944	0.0480	0.0025	90	100	119.0	5.9	119.9	3.0	409	279	0.68
20	0.1344	0.0060	0.0189	0.0004	0.2450	0.0519	0.0023	229	94	128.1	5.5	120.5	2.7	504	377	0.75
21	0.1236	0.0054	0.0185	0.0004	0.1627	0.0485	0.0021	104	90	117.8	4.9	118.3	2.5	568	396	0.70
22	0.1238	0.0066	0.0189	0.0006	0.2921	0.0476	0.0024	70	100	117.9	6.0	120.5	3.5	419	339	0.81
23	0.1268	0.0093	0.0185	0.0005	0.0179	0.0504	0.0039	100	150	119.8	8.4	117.8	3.4	181	148	0.82
24	0.1200	0.0078	0.0184	0.0005	0.0888	0.0480	0.0032	20	130	114.2	7.0	117.4	3.0	254	221	0.87
25	0.1231	0.0095	0.0185	0.0005	0.1911	0.0485	0.0038	20	140	116.5	8.5	118.2	3.2	189	155	0.82
26	0.1282	0.0084	0.0186	0.0005	0.2125	0.0503	0.0033	120	130	121.4	7.5	118.6	3.1	386	435	1.13

TABLE 3 Zircon trace element data for zircons from Dazeshan magmatic rocks.

	Age	P	Ti	Y	Nb	La	Ce	Pr	Nd	Sm	Eu	Gd	Tb	Dy	Ho	Er	Tm	Yb	Lu	Hf
DZS_1A_3	120.1	440	7.6	3,600	15.3	0.005	51.4	0.083	1.66	8.61	5.52	64.3	23.6	304	117	559	115	1,034	200	11,160
DZS_1A_4	117.5	200	5.7	1,648	2.8	0.037	32.7	0.143	2.78	6.49	3.69	35.8	11.8	141	53.1	255	53.1	475	97.1	10,180
DZS_1A_6	120.1	260	8.5	1,680	2.0	0.036	48.4	0.294	4.72	10.1	5.75	49.6	14.6	155	56.1	264	51.6	467	97.2	9,170
DZS_1A_7	117.9	326	5.4	1,519	1.5	0.001	37.0	0.162	2.71	5.48	3.31	31.6	10.1	126	48.1	244	52.2	470	103	8,650
DZS_1A_8	118.1	302	4.5	2040	3.2	0.003	26.1	0.093	1.22	5.37	3.12	35.0	12.4	168	65.9	346	69.4	620	128	10,810
DZS_1A_9	117.7	245	8.9	1700	2.9	0.002	45.9	0.161	3.21	7.31	4.04	41.8	13.1	159	56.7	269	55.0	481	100	9,440
DZS_1A_10	118.3	152	4.6	976	1.0	0.050	20.6	0.164	3.21	5.81	2.95	25.9	7.57	88.6	31.9	151	31.5	284	58.6	9,950
DZS_1A_11	116.4	207	8.9	1,524	2.9	0.041	36.3	0.126	1.98	4.40	2.66	27.9	10.1	127	48.7	246	49.7	450	95.1	9,730
DZS_1A_12	117.3	329	10.2	4,190	35.0	—	58.9	0.093	2.30	13.1	7.83	94.6	33.2	395	140	606	117	934	171	13,710
DZS_1A_14	117.1	230	4.2	1,230	1.3	0.013	24.6	0.180	3.68	6.80	3.43	30.6	9.39	110	39.9	190	42.0	376	79.2	9,970
DZS_1A_15	118.2	301	8.6	3,690	15.2	—	47.2	0.066	1.58	7.13	5.56	63.4	23.8	311	121	576	115	1,005	194	12,110
DZS_1A_16	119.5	312	9.3	3,860	32.5	0.052	52.5	0.096	1.91	10.6	6.77	77.5	28.6	358	129	580	110	924	166	13,360
DZS_1A_18	120.5	217	10.0	2,595	7.3	—	50.1	0.097	1.86	5.69	4.10	47.1	17.3	221	86.3	409	80.5	718	143	10,920
DZS_1A_19	125.1	192	8.8	1,607	3.6	0.042	39.1	0.162	2.97	5.94	2.92	32.1	11.3	140	54.1	256	52.7	489	99.2	9,870
DZS_1A_20	121.8	272	11.3	2,880	16.0	—	61.1	0.109	2.66	9.23	5.86	64.6	21.5	261	96.4	441	86.4	759	143	11,110
DZS_1A_21	122.5	281	10.2	1884	2.5	0.018	59.9	0.288	5.38	9.34	5.05	48.6	14.4	175	65.7	300	61.5	561	117	8,710
DZS_1A_22	122.4	249	5.3	1,310	1.6	0.008	25.4	0.155	3.01	5.09	3.10	28.6	8.76	110	41.1	209	44.5	430	89.2	9,710
DZS_1A_23	124.8	191	7.9	1,362	3.7	0.002	28.3	0.090	1.49	4.03	2.42	26.1	9.34	115	46.6	227	47.4	406	88.4	9,970
DZS_1A_24	118.3	212	10.1	1,294	2.3	—	35.1	0.112	2.09	4.29	2.55	26.6	9.03	112	41.7	201	44.2	394	84.3	9,280
DZS_1A_26	119.3	176	7.2	1,006	1.7	—	24.1	0.098	1.59	3.28	1.87	20.5	6.74	84.4	34.2	165	34.3	312	65.2	9,390
DZS_1A_27	116.7	254	5.1	1829	2.0	0.033	48.8	0.473	7.70	13.0	7.07	56.9	15.6	179	60.5	283	58.2	545	107	10,170
DZS_2A_1	141.0	333	4.6	3,112	42.3	—	36.6	0.02	0.69	5.22	1.73	47.6	18.5	264	104	472	88.1	752	139	14,600
DZS_2A_2	138.2	556	6.0	3,990	37.4	—	41.5	0.05	1.81	8.49	1.57	69.6	25.8	355	131	568	107	843	152	15,900
DZS_2A_3	144.9	347	5.5	3,370	48.7	0.02	41.0	0.05	1.08	5.12	1.73	45.4	19.1	277	107	510	98.7	840	151	14,170
DZS_2A_4	144.8	385	10.3	5,700	36.6	—	47.6	0.07	2.09	10.9	4.43	102	38.0	492	189	825	152	1,233	213	12,450
DZS_2A_5	139.6	627	9.2	5,810	97.1	0.40	72.7	0.34	3.64	11.5	2.72	91.5	36.3	501	185	826	149	1,212	203	14,680

(Continued on following page)

TABLE 3 (*Continued*) Zircon trace element data for zircons from Dazeshan magmatic rocks.

	Age	P	Ti	Y	Nb	La	Ce	Pr	Nd	Sm	Eu	Gd	Tb	Dy	Ho	Er	Tm	Yb	Lu	Hf
DZS_2A_8	137.7	288	7.8	3,121	33.2	—	40.5	0.05	1.86	7.83	2.99	58.9	22.2	278	103	455	85.9	678	125	13,210
DZS_2A_10	138.8	408	3.6	3,410	7.75	—	18.8	0.04	1.16	4.84	2.23	47.5	19.0	272	107	519	102	862	161	12,640
DZS_2A_11	143.9	499	3.7	4,330	14.2	—	22.0	0.03	0.65	5.37	2.23	49.9	22.4	330	137	674	138	1,206	229	12,260
DZS_2A_12	136.5	154	5.5	1772	2.08	0.00	9.22	0.10	1.88	4.94	3.09	35.2	11.8	148	56.1	262	49.7	428	84.9	10,220
DZS_2A_13	144.8	286	6.0	3,570	30.6	—	28.6	0.03	0.88	4.36	1.36	43.3	19.0	278	113	541	105	888	161	13,370
DZS_2A_15	147.9	391	2.9	2,790	12.6	—	16.8	0.02	0.51	3.37	1.10	34.6	15.3	223	90.5	438	87.2	765	143	12,940
DZS_2A_16	141.9	286	0.9	1,483	11.0	—	5.49	0.00	0.23	1.41	0.32	15.7	7.26	110	45.9	240	52.6	482	92.5	18,250
DZS_2A_18	139.7	344	17.9	3,850	33.2	0.01	60.2	0.39	7.90	17.2	6.87	98.3	31.1	349	122	534	97.4	778	138	12,090
DZS_2A_21	145.0	354	–	1,654	27.8	—	5.57	—	—	0.90	0.18	14.3	7.35	115	55.7	289	69.4	641	125	23,950
DZS_2A_22	137.7	253	12.9	2,750	11.7	—	51.5	0.15	3.27	8.91	5.84	54.3	18.7	242	95.1	444	94.1	869	171	9,610
DZS_2A_23	146.2	349	1.3	1831	32.1	—	5.63	—	—	1.11	0.20	15.8	8.52	133	55.7	319	77.0	712	140	23,900
DZS_2A_7	2078	336	5.4	996	5.10	—	17.7	0.06	1.36	2.96	0.36	21.3	7.24	90.3	34.1	161	33.1	289	58.6	10,750
DZS_2A_9	1838	198	6.1	253	0.35	—	4.09	0.03	0.33	0.90	0.09	4.94	1.92	22.0	8.42	39.2	7.98	72.2	14.9	12,150
DZS_2A_25	1826	531	4.9	1,281	8.96	—	11.6	0.02	0.54	1.96	0.38	18.3	7.86	108	44.6	225	47.2	421	81.5	11,970
DZS_2A_14	149.4	200	1.6	934	8.28	—	4.44	0.02	0.28	1.08	0.64	9.93	4.54	68.0	29.9	155	32.4	294	61.5	21,850
DZS_2A_17	160.2	563	4.1	3,850	28.5	1.72	27.1	1.03	6.73	6.62	1.52	47.0	21.3	287	120	584	113	989	175	15,540
DZS_2A_19	921.0	420	4.4	2,140	12.2	2.00	25.7	0.90	5.50	4.24	1.13	29.8	12.4	177	70.5	332	67.4	604	109	13,350
DZS_2A_20	206.0	337	6.0	2,510	5.37	0.06	13.4	0.07	1.08	4.32	2.05	36.7	14.0	198	78.8	396	78.4	735	133	10,230
DZS_2A_24	423.0	277	4.9	2,590	19.3	—	26.6	0.05	1.07	4.70	1.23	38.4	15.6	209	86.5	401	79.9	739	126	13,680
DZS_3A_2	119.8	112	3.9	734	4.05	—	36.7	0.05	0.82	2.35	0.84	13.1	4.20	53.6	21.1	112	26.7	270	60.6	10,810
DZS_3A_3	119.5	69.0	2.9	612	1.66	—	30.4	0.06	1.84	3.30	1.42	16.5	4.73	51.8	19.8	91.9	20.1	197	39.3	11,420
DZS_3A_4	121.4	51.0	1.8	526	3.21	0.00	22.9	0.03	0.52	1.07	0.41	6.89	2.35	29.8	13.1	75.6	20.6	238	57.0	14,130
DZS_3A_5	119.6	138	4.7	926	4.75	0.01	56.3	0.11	1.84	3.71	1.48	19.5	6.05	72.7	28.0	137	30.4	309	67.0	10,640
DZS_3A_6	121.3	167	2.1	848	5.02	—	30.8	0.03	0.57	1.48	0.54	9.69	3.44	46.9	21.5	127	32.6	367	92.0	12,760
DZS_3A_7	119.2	114	3.5	763	4.13	—	45.4	0.07	1.16	3.07	1.05	15.7	5.10	60.4	22.9	118	26.1	265	58.2	10,870
DZS_3A_8	122.6	288	5.1	1,085	2.71	0.02	56.5	0.26	3.76	6.75	2.60	30.9	8.66	96.7	34.0	154	31.3	292	57.1	10,220

TABLE 3 (*Continued*) Zircon trace element data for zircons from Dazeshan magmatic rocks.

	Age	P	Ti	Y	Nb	La	Ce	Pr	Nd	Sm	Eu	Gd	Tb	Dy	Ho	Er	Tm	Yb	Lu	Hf
DZS_3A_9	119.1	236	8.8	1,661	1.64	0.12	56.4	0.84	11.2	16.8	6.57	68.5	16.7	175	55.0	226	44.8	383	75.4	8,410
DZS_3A_10	120.5	123	3.4	1,461	7.41	0.01	59.4	0.13	2.39	5.25	1.64	26.8	7.91	95.7	40.2	209	51.0	513	115	11,960
DZS_3A_11	120.3	189	4.8	1805	10.5	0.45	79.8	0.33	3.68	6.59	2.02	33.2	10.1	130	50.8	252	62.1	618	132	11,160
DZS_3A_12	119.5	165	3.2	759	2.36	0.03	33.6	0.13	1.52	3.20	1.37	15.8	4.91	58.0	22.0	110	26.2	254	58.4	11,520
DZS_3A_13	117.8	132	3.3	683	3.15	0.01	28.7	0.04	1.09	2.60	0.83	12.2	3.92	48.6	20.6	103	25.7	266	63.3	11,890
DZS_3A_14	119.9	191	4.4	1,072	4.11	0.12	65.5	0.22	3.65	6.72	2.03	27.5	8.51	94.0	34.3	165	35.1	322	66.6	11,180
DZS_3A_15	124.3	125	4.2	1,582	17.3	0.03	79.1	0.09	1.36	2.96	1.02	19.0	6.99	96.6	43.0	238	60.8	670	151	12,830
DZS_3A_16	120.1	122	3.5	812	4.50	0.04	38.5	0.08	1.32	2.84	1.08	16.9	5.16	63.5	24.9	125	29.0	285	63.8	11,240
DZS_3A_17	119.0	131	2.0	993	4.34	0.03	26.3	0.07	1.01	3.29	1.18	18.1	5.95	71.1	26.8	146	33.5	361	77.1	13,170
DZS_3A_18	120.9	116	3.2	981	6.78	—	48.3	0.07	1.38	3.00	1.01	17.0	5.51	70.6	28.5	146	36.9	384	83.5	11,970
DZS_3A_19	118.8	131	4.2	808	4.29	—	44.2	0.08	1.18	2.72	1.21	15.8	5.18	65.0	24.8	124	27.1	272	58.2	10,510
DZS_3A_20	120.8	130	2.1	760	2.29	—	23.7	0.07	1.16	3.02	1.17	15.2	4.54	55.2	22.4	119	29.6	316	66.9	13,010
DZS_3A_21	122.4	304	9.3	1,260	3.80	0.07	76.2	0.34	4.39	8.01	2.90	36.6	9.64	115	40.3	189	38.7	360	69.6	8,800
DZS_3A_23	121.7	147	4.3	1,117	2.00	0.01	54.8	0.27	4.40	9.07	2.91	38.9	9.98	107	37.8	172	35.4	305	60.9	10,170
DZS_3A_24	122.8	129	4.5	743	3.72	0.11	54.3	0.12	1.64	3.29	1.28	18.1	5.18	64.7	24.7	116	27.2	252	49.8	9,970
DZS_3A_25	121.5	123	4.1	806	5.08	0.01	46.6	0.08	1.50	2.82	1.16	15.9	5.35	66.1	25.3	131	29.5	308	61.4	10,000
DZS_3A_26	121.9	221	7.4	1822	1.69	0.11	72.6	1.06	14.2	22.1	7.66	84.2	20.2	207	64.1	260	49.9	452	79.9	8,330
DZS_4A_1	120.3	106	2.9	714	3.50	—	41.5	0.06	1.18	2.78	0.88	14.5	4.80	56.4	21.5	113	24.4	238	52.2	11,420
DZS_4A_2	122.6	188	4.0	670	2.54	0.01	45.7	0.10	1.69	3.31	1.13	14.9	5.10	60.4	21.1	104	21.9	210	42.9	10,470
DZS_4A_3	118.3	157	2.6	2,331	22.4	0.30	73.4	0.16	1.70	4.00	0.88	27.7	10.4	139	61.5	353	88.9	966	214	14,730
DZS_4A_4	119.1	132	3.3	1,128	3.83	0.02	54.7	0.17	2.96	5.09	1.90	29.0	8.28	97.2	34.9	167	34.9	329	67.6	10,800
DZS_4A_5	118.3	127	3.2	896	5.67	0.13	42.7	0.14	1.59	3.37	1.11	18.2	5.41	66.9	26.3	137	31.9	312	69.2	11,940
DZS_4A_6	119.9	287	5.9	1819	6.74	0.04	135	0.46	7.45	13.0	3.69	59.4	16.1	182	61.1	274	53.4	491	94.9	9,440
DZS_4A_8	122.9	87.0	3.3	1,232	10.9	0.02	47.7	0.06	0.93	2.50	0.72	15.5	5.84	80.3	33.7	197	47.3	501	108	11,710
DZS_4A_9	119.1	108	2.7	872	5.63	0.04	55.2	0.08	1.27	3.00	0.93	15.8	5.08	66.0	24.7	128	29.4	281	61.3	11,470
DZS_4A_10	118.7	154	3.9	901	4.70	0.00	56.6	0.09	1.71	3.83	1.23	20.7	6.31	74.6	29.3	149	33.1	305	62.9	10,440

TABLE 3 (*Continued*) Zircon trace element data for zircons from Dazeshan magmatic rocks.

	Age	P	Ti	Y	Nb	La	Ce	Pr	Nd	Sm	Eu	Gd	Tb	Dy	Ho	Er	Tm	Yb	Lu	Hf
DZS_4A_11	119.1	270	2.1	1,388	13.2	0.01	62.8	0.05	0.91	2.17	0.43	13.6	5.31	78.2	36.1	216	59.0	683	151	13,610
DZS_4A_13	120.8	174	3.4	1,688	5.69	0.26	54.7	0.29	4.57	6.74	2.19	35.3	11.1	127	49.8	256	55.5	547	117	11,460
DZS_4A_14	119.1	199	2.1	710	5.47	—	22.6	0.03	0.37	1.22	0.26	8.10	2.99	41.2	17.4	113	28.6	316	70.8	12,530
DZS_4A_15	118.9	370	4.3	970	4.01	0.02	55.5	0.13	2.02	3.97	1.17	21.8	6.87	79.5	29.2	145	32.6	320	65.0	10,430
DZS_4A_16	123.1	190	4.8	1,332	7.85	0.01	76.7	0.13	2.71	5.83	1.43	29.3	9.47	109	41.7	203	47.2	431	89.6	10,780
DZS_4A_17	120.5	126	3.7	1999	9.92	0.26	60.2	0.40	5.34	8.70	2.43	42.2	12.4	152	57.5	305	70.6	736	148	12,640
DZS_4A_19	124.4	179	3.5	1,102	4.40	—	44.1	0.13	2.31	5.15	1.34	25.1	7.43	88.9	31.8	162	39.5	388	73.4	11,360
DZS_4A_20	120.6	255	4.5	888	2.60	0.01	44.4	0.14	2.15	4.62	1.32	21.4	6.43	74.9	29.8	134	31.8	265	53.4	10,730
DZS_4A_21	119.0	125	4.0	720	3.81	0.10	39.5	0.10	1.34	2.88	0.88	15.4	4.88	61.2	22.0	111	26.5	250	51.5	11,020
DZS_4A_22	119.9	135	3.8	826	5.12	—	47.6	0.08	1.28	3.24	0.95	16.1	5.27	67.7	25.1	129	29.8	290	58.5	10,500
DZS_4A_23	120.5	110	3.3	737	5.62	0.10	47.9	0.08	1.12	2.62	0.63	13.4	4.39	54.6	21.3	115	27.5	279	55.9	11,630
DZS_4A_24	118.3	145	4.4	1,108	7.26	0.08	60.5	0.10	1.59	3.40	1.09	21.6	6.89	86.6	34.8	173	41.3	413	81.6	10,820
DZS_4A_25	120.5	132	3.6	1,084	3.15	0.01	47.2	0.14	3.44	5.97	1.88	27.7	8.45	97.7	36.0	166	38.2	368	68.0	10,890
DZS_4A_26	117.8	313	4.7	666	2.19	—	44.4	0.12	1.76	3.85	1.09	17.4	5.73	60.8	20.9	102	21.7	208	38.3	9,320
DZS_4A_27	117.4	222	5.9	1,043	4.47	0.02	78.2	0.17	2.74	5.94	1.71	26.7	7.50	91.1	32.6	159	34.9	308	60.3	9,720
DZS_4A_28	118.2	423	4.1	727	2.29	4.60	59.4	1.56	9.00	4.97	1.47	20.6	6.34	63.8	23.5	115	24.5	235	42.5	9,850
DZS_4A_29	118.6	286	4.5	1,586	2.92	0.87	82.4	0.82	10.0	14.5	3.83	59.4	14.8	160	55.7	247	50.7	448	78.8	10,410

TABLE 4 Zircon Hf isotope data for the rhyolite porphyry and Dazeshan biotite granite.

Spot no.	$^{176}Yb/^{177}Hf$	2σ	$^{176}Lu/^{177}Hf$	2σ	$^{176}Hf/^{177}Hf$	2σ	$\varepsilon Hf\ (t)$	T_{DM1} (Ma)	T_{DM2} (Ma)	$f_{Lu/Hf}$	Age
DZS-3A-2	0.042275	0.000167	0.001093	0.000005	0.282177	0.000015	−18.5	1,521	3,290	−0.9671	119.8
DZS-3A-4	0.033602	0.000317	0.000916	0.000009	0.282133	0.000013	−20.0	1,575	3,425	−0.9724	121.4
DZS-3A-5	0.031352	0.000349	0.000776	0.000008	0.282175	0.000014	−18.5	1,510	3,292	−0.9766	119.6
DZS-3A-6	0.038969	0.000316	0.001067	0.000007	0.282181	0.000013	−18.3	1,513	3,273	−0.9679	121.3
DZS-3A-9	0.039306	0.000836	0.000937	0.000019	0.282181	0.000015	−18.4	1,508	3,276	−0.9718	119.1
DZS-3A-11	0.040962	0.000431	0.001003	0.000010	0.282140	0.000014	−19.8	1,568	3,404	−0.9698	120.3
DZS-4A-1	0.027038	0.000154	0.000678	0.000005	0.282195	0.000017	−17.8	1,479	3,229	−0.9796	120.3
DZS-4A-6	0.035255	0.000556	0.000911	0.000014	0.282161	0.000015	−19.0	1,536	3,336	−0.9726	122.9
DZS-4A-8	0.038623	0.000698	0.000964	0.000019	0.282130	0.000013	−20.2	1,580	3,436	−0.9710	119.1
DZS-4A-9	0.036108	0.000394	0.000882	0.000011	0.282147	0.000015	−19.6	1,554	3,385	−0.9734	118.7
DZS-4A-10	0.041680	0.000512	0.000988	0.000012	0.282141	0.000013	−19.8	1,566	3,402	−0.9702	119.9
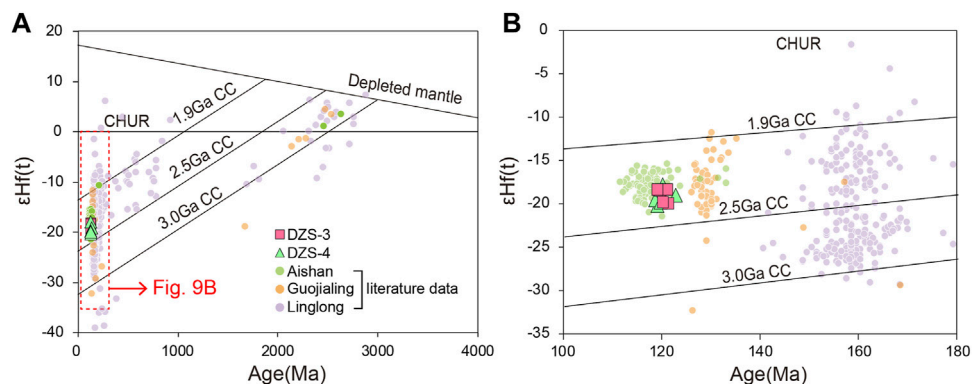
FIGURE 9
Zircon Hf isotopic data from rhyolite porphyry **(A)** and Dazeshan biotite granite **(B)**. Published zircon isotope data are compiled from Yang et al. (2012; 2017), Ma et al. (2013; 2014), and Li et al. (2019).
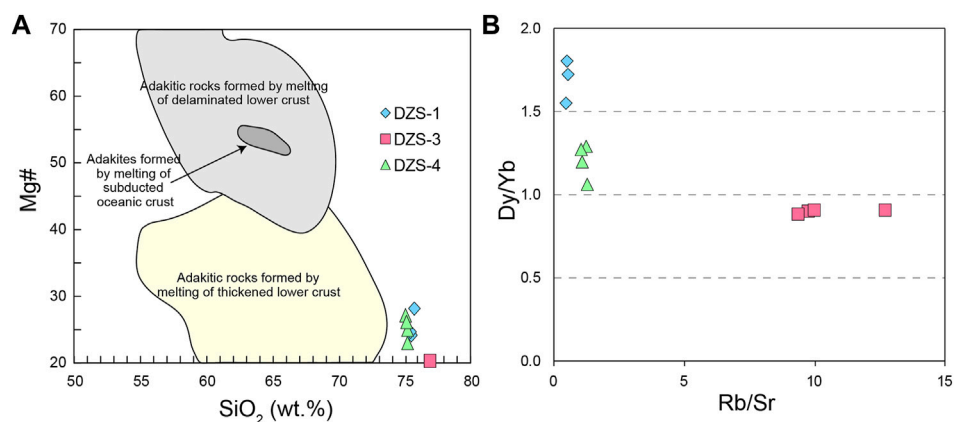
FIGURE 10
Mg# vs. SiO$_2$ **(A)** and Dy/Yb vs. Rb/Sr **(B)** diagrams. Adakite fields are adopted from Sen and Dunn (1994), Rapp and Watson (1995), and Rapp et al. (1999) and references therein.

melting of the lower crust with subsequent fractionation crystallization.

5.2 Multiple reworking events of the NCC lower crust

Previous studies have shown that the widely distributed Jurassic Linglong granite in the Jiaodong Penisular has adakite-like geochemical signatures with high Sr/Y and La/Yb ratios, which were considered to be the result of the melting of the thickened lower crust at the garnet stability field (Ma et al., 2013; Yang et al., 2017). The geodynamic model for the crustal thickening is probably related to the

subduction of the Paleo-Pacific plate (Wu et al., 2005b; Ma et al., 2013). This left a residue with large portions of garnet in the lower crust, which by inference should be depleted of LILE and LREE due to the prior melt extraction. The crust-mantle interaction was strikingly extensive during the Early Cretaceous (~130 Ma) given the widespread granitic and/or mafic magmatism and extensional deformation-related sedimentary basins (Wu et al., 2005b; Cai et al., 2013; Yang et al., 2018a, b; Meng et al., 2019). Furthermore, the ~130 Ma granitic rocks in Jiaodong (e.g., Guojialing pluton), which also show adakite-like characters, were interpreted to be derived either from the melting of the delaminated eclogitic crust (Hou et al., 2007) or multi-stage magma mixing between Archean lower crust derived felsic magma
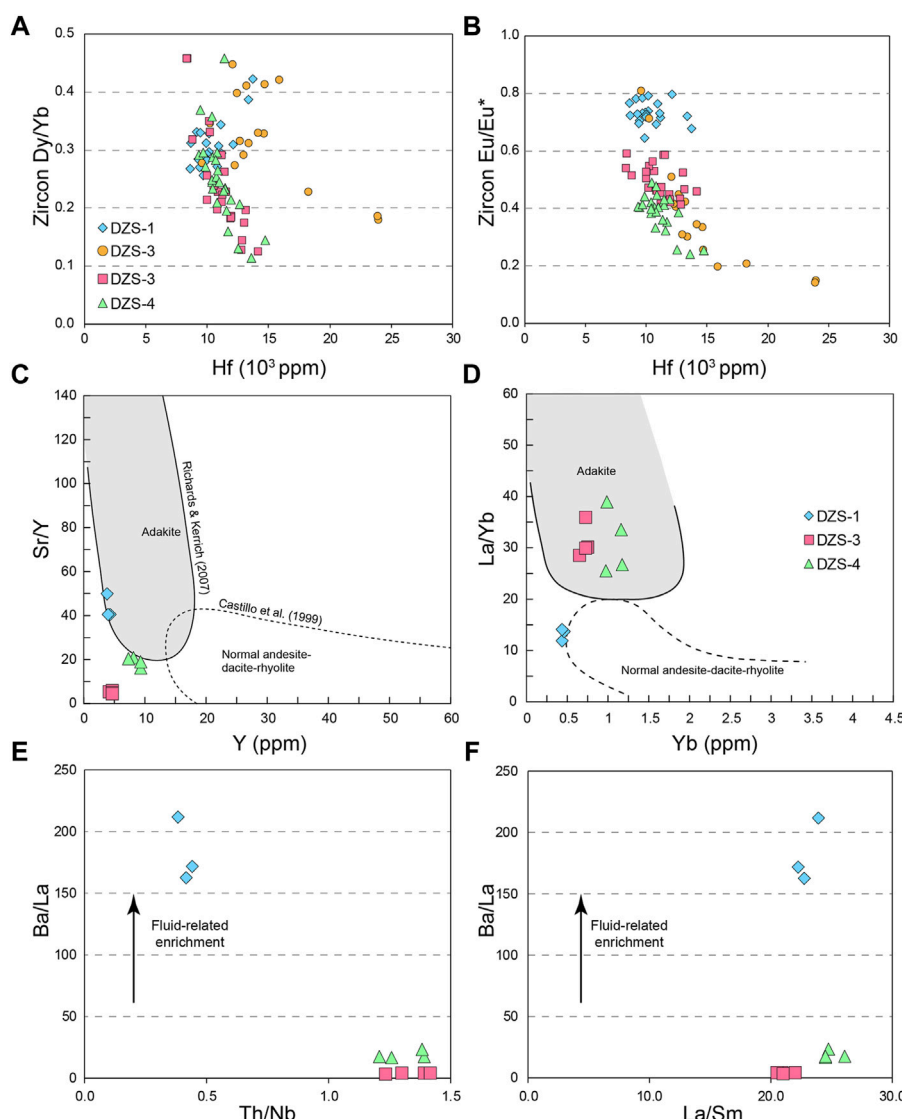
FIGURE 11
Zircon Dy/Yb **(A)** and Eu/Eu* **(B)** vs. Hf contents for the studied magmatic rocks. **(C)** Sy/Y vs. Y plot. The adakite and normal andesite-dacite-rhyolite fields are from Richards and Kerrich (2007) and Castillo et al. (1999), respectively. **(D)** La/Yb vs. Yb plot. Ba/La vs. Th/Nb **(E)** and La/Sm **(F)** plots. See the text for explanation.

and mafic lower crust-derived dioritic magma (Jiang et al., 2016).

The three intrusions are emplaced at around 120 Ma based on the zircon U-Pb ages obtained in the present study (Figure 7). These magmatic rocks were derived from the melting of the ancient lower crust of the NCC, as discussed in the previous section. The strontium concentrations for these samples (<200 ppm) are not as high as those in the Linglong and Guojialing magmatic rocks reported by Yang et al. (2012) (>300 ppm). Consequently, the Sr/Y values of the quartz porphyry, rhyolite porphyry, and the Dazeshan biotite granite are low (Figure 11C), unlike the Jurassic and Early

Cretaceous granitoids in Jiaodong. However, the La/Yb ratios are high and plot within the "adakite field" (Figure 11D) (Condie, 2005; Castillo, 2006). This antinomy can be explained by the dominant crystal fractionation of amphibole and plagioclase during the magmatic evolution. As mentioned above, limited crystal fractionation occurred in the parent magma of the quartz porphyry. Therefore, the Sr/Y and La/Yb ratios probably represent its original character in these magmatic rocks. The low Sr/Y and La/Yb ratios (<50 and <15, respectively; Figures 11C, D), imply that little or no garnet remained as a residue phase in the source. Thus, the quartz porphyry may have been derived

from a shallow crustal level rather than a thickened lower crust (>50 km) as in Linglong granite. Fluid flux played an important role in inducing the melting reaction because the Ba/La ratios for these samples are elevated (Figures 11E, F). Barium is a fluid mobile element, while the La is less so (Kessel et al., 2005). Therefore, the subduction-related fluid carried more Ba than La and generated high Ba/La ratios in the resultant magma.

The rhyolite porphyry and Dazeshan biotite granite, however, experienced amphibole + plagioclase fractionation, as evidenced by the geochemical data. Both suites have low Sr/Y but high La/Yb ratios. We propose that the plagioclase fractionation depleted the Sr concentration in the remnant melt but did not affect the La or Yb contents of the magma. Garnet, which retains most of the Y and Yb in the source, should have been stable when the parent magma of the rhyolite porphyry and the Dazeshan biotite granite formed. Under such a scenario, these two suites were probably generated by melting of a thicker crust compared to the quartz porphyry. These two suites were most likely formed by dehydration melting considering the low Ba/La but high Th/Nb and La/Sm ratios in these samples. Thorium is more incompatible than Nb while La is more incompatible than Sm; thus, Th/Nb and La/Sm ratios would be promoted during dehydration melting when no external element is introduced into the system.

Therefore, the melting may have occurred at different crustal levels at around 120 Ma, with distinct triggers. The fluid responsible for the fluxed melting very likely originated from the upwelling mafic magma, which was ultimately sourced from the dehydration of the subducted Paleo-Pacific plate (Windley et al., 2010; Geng et al., 2019). The dehydration melting in the case of rhyolite porphyry and the Dazeshan biotite granite may have been induced by heat loss from the underplated mafic magma. Regardless of fluid fluxed or dehydration melting, this change required a deeper source of heat and fluid. This required water-rich mafic magma, among which lithosphere mantle-derived magma is a possible candidate (Geng et al., 2019).

6 Conclusion

The results of this study reveal that the magmatic rocks in the Dazeshan region have zircon ages of ~120 Ma and were generated by crustal melting; however, they experienced different melting/differentiation processes. The quartz porphyry was formed by fluid-mediated melting without apparent crystal crystallization. The rhyolite porphyry and the Dazeshan biotite granite were produced by dehydration melting and underwent amphibole and plagioclase fractionation, as

indicated by whole-rock and zircon trace element data. Our results imply that, in the Early Cretaceous, the lower crust of the NCC was reworked multiple times in different ways. The driving force for the reworking probably invoked the underplating of water-rich mafic magma under an extensional regime (Li et al., 2012), which not only provided fluid to generate the quartz porphyry but also released heat to promote the dehydration melting of the lower crust to form the rhyolite porphyry and biotite granite.

Data availability statement

The original contributions presented in the study are included in the article/Supplementary Material. Further inquiries can be directed to the corresponding author.

Author contributions

LD collected samples, performed whole-rock and zircon geochemical analyses, and wrote the manuscript. XB drew the maps and figures. CD performed the data processing. ZY reviewed and edited the manuscript.

Funding

Acknowledgments

Conflict of interest

CD was employed in the Postdoctoral Programme of the Guosen Securities company.

The remaining authors declare that the research was conducted in the absence of any commercial or financial relationships that could be construed as a potential conflict of interest.

Publisher's note

All claims expressed in this article are solely those of the authors and do not necessarily represent those of their affiliated organizations, or those of the publisher, the editors, and the reviewers. Any product that may be evaluated in this article, or claim that may be made by its manufacturer, is not guaranteed or endorsed by the publisher.

References

Brown, M. (2013). Granite: From Genesis to emplacement. *Geol. Soc. Am. Bull.* 125, 1079–1113. doi:10.1130/b30877.1

Cai, Y. C., Fan, H. R., Santosh, M., Liu, X., Hu, F. F., Yang, K. F., et al. (2013). Evolution of the lithospheric mantle beneath the southeastern North China Craton: Constraints from mafic dikes in the Jiaobei terrain. *Gondwana Res.* 24, 601–621. doi:10.1016/j.gr.2012.11.013

Cao, K., Yang, Z. M., White, N. C., and Hou, Z. Q. (2022). Generation of the giant porphyry Cu-Au deposit by repeated recharge of mafic magmas at Pulang in eastern Tibet. *Econ. Geol.* 117, 57–90. doi:10.5382/econgeo.4860

Castillo, P. R. (2006). An overview of adakite petrogenesis. *Chin. Sci. Bull.* 51, 257–268. doi:10.1007/s11434-006-0257-7

Castillo, P. R., Janney, P. E., and Solidum, R. U. (1999). Petrology and geochemistry of Camiguin Island, southern Philippines: Insights to the source of adakites and other lavas in a complex arc setting. *Contributions mineralogy petrology* 134, 33–51. doi:10.1007/s004100050467

Chappell, B. (2004). Towards a unified model for granite Genesis. *Earth Environ. Sci. Trans. R. Soc. Edinb.* 95, 1–10. doi:10.1017/s0263593300000870

Charles, N., Gumiaux, C., Augier, R., Chen, Y., Faure, M., Lin, W., et al. (2012). Metamorphic core complex dynamics and structural development: Field evidences from the Liaodong Peninsula (China, East Asia). *Tectonophysics* 560-561, 22–50. doi:10.1016/j.tecto.2012.06.019

Chen, J. F., Xie, Z., Zhang, X. D., Zhou, T. X., Park, Y. S., Ahn, K. S., et al. (2003). U-Pb zircon ages for a collision-related K-rich complex at Shidao in the Sulu ultrahigh pressure terrane, China. *Geochem. J.* 37, 35–46. doi:10.2343/geochemj.37.35

Chen, L., Tao, W., Zhao, L., and Zheng, T. (2008). Distinct lateral variation of lithospheric thickness in the Northeastern North China Craton. *Earth Planet. Sci. Lett.* 267, 56–68. doi:10.1016/j.epsl.2007.11.024

Clemens, J. D., Stevens, G., and Bryan, S. E. (2020). Conditions during the formation of granitic magmas by crustal melting-hot or cold; drenched, damp or dry? *Earth-Science Rev.* 200, 102982. doi:10.1016/j.earscirev.2019.102982

Condie, K. C. (2005). TTGs and adakites: Are they both slab melts? *Lithos* 80, 33–44. doi:10.1016/j.lithos.2003.11.001

Davidson, J., Turner, S., Handley, H., Macpherson, C., and Dosseto, A. (2007). Amphibole "sponge" in arc crust? *Geol.* 35, 787–790. doi:10.1130/g23637a.1

DePaolo, D. J. (1981). Trace element and isotopic effects of combined wallrock assimilation and fractional crystallization. *Earth Planet. Sci. Lett.* 53, 189–202. doi:10.1016/0012-821x(81)90153-9

Gao, P., Zheng, Y. F., and Zhao, Z. F. (2016). Experimental melts from crustal rocks: A lithochemical constraint on granite petrogenesis. *Lithos* 266–267, 133–157. doi:10.1016/j.lithos.2016.10.005

Gao, S., Rudnick, R. L., Yuan, H. L., Liu, X. M., Liu, Y. S., Xu, W. L., et al. (2004). Recycling lower continental crust in the North China craton. *Nature* 432, 892–897. doi:10.1038/nature03162

Geng, X., Foley, S. F., Liu, Y., Wang, Z., Hu, Z., and Zhou, L. (2019). Thermal-chemical conditions of the North China Mesozoic lithospheric mantle and implication for the lithospheric thinning of cratons. *Earth Planet. Sci. Lett.* 516, 1–11. doi:10.1016/j.epsl.2019.03.012

Goss, S. C., Wilde, S. A., Wu, F., and Yang, J. (2010). The age, isotopic signature and significance of the youngest mesozoic granitoids in the Jiaodong terrane, Shandong province, north China craton. *Lithos* 120, 309–326. doi:10.1016/j.lithos.2010.08.019

Hou, M. L., Jiang, Y. H., Jiang, S. Y., Ling, H. F., and Zhao, K. D. (2007). Contrasting origins of late mesozoic adakitic granitoids from the northwestern Jiaodong Peninsula, east China: Implications for crustal thickening to delamination. *Geol. Mag.* 144, 619–631. doi:10.1017/s0016756807003494

Jahn, B. M., and Zhang, Z. Q. (1984). Archean granulite gneisses from eastern Hebei province, China: Rare Earth geochemistry and tectonic implications. *Contr. Mineral. Pet.* 85, 224–243. doi:10.1007/bf00378102

Jiang, P., Yang, K. F., Fan, H. R., Liu, X., Cai, Y. C., and Yang, Y. H. (2016). Titanite-scale insights into multi-stage magma mixing in early cretaceous of NW Jiaodong terrane, north China craton. *Lithos* 258–259, 197–214. doi:10.1016/j.lithos.2016.04.028

Kessel, R., Schmidt, M. W., Ulmer, P., and Pettke, T. (2005). Trace element signature of subduction-zone fluids, melts and supercritical liquids at 120–180 km depth. *Nature* 437, 724–727. doi:10.1038/nature03971

Le Bas, M. J., Le Maitre, R. W., Streckeisen, A., and Zanettin, B. (1986). A chemical classification of volcanic rocks based on the total alkali – silica diagram. *J. Petrology* 27, 745–750. doi:10.1093/petrology/27.3.745

Lee, C. T. A., Luffi, P., and Chin, E. J. (2011). Building and destroying continental mantle. *Annu. Rev. Earth Planet. Sci.* 39, 59–90. doi:10.1146/annurev-earth-040610-133505

Li, X. C., Fan, H. R., Santosh, M., Hu, F. F., Yang, K. F., Lan, T. G., et al. (2012). An evolving magma chamber within extending lithosphere: An integrated geochemical, isotopic and zircon U-Pb geochronological study of the Gushan granite, eastern North China Craton. *J. Asian Earth Sci.* 50, 27–43. doi:10.1016/j.jseaes.2012.01.016

Li, X. H., Fan, H. R., Hu, F. F., Hollings, P., Yang, K. F., and Liu, X. (2019). Linking lithospheric thinning and magmatic evolution of late Jurassic to early cretaceous granitoids in the Jiaobei Terrane, southeastern North China Craton. *Lithos* 324–325, 280–296. doi:10.1016/j.lithos.2018.11.022

Liu, D. Y., Nutman, A. P., Compston, W., Wu, J. S., and Shen, Q. H. (1992). Remnants of ≥3800 Ma crust in the Chinese part of the Sino-Korean craton. *Geol.* 20, 339–342. doi:10.1130/0091-7613(1992)020<0339:romcit>2.3.co;2

Liu, Y., Gao, S., and Tingchuan, L. (1999). Geochemistry of granulites in north China craton: Implications for the composition of archean lower crus. *Geology-Geochemistry* 27, 40–46.

Liu, Y., Gao, S., Yuan, H., Zhou, L., Liu, X., Wang, X., et al. (2004). U-Pb zircon ages and Nd, Sr, and Pb isotopes of lower crustal xenoliths from north China craton: Insights on evolution of lower continental crust. *Chem. Geol.* 211, 87–109. doi:10.1016/j.chemgeo.2004.06.023

Liu, Y. S., Gao, S., Jin, S. Y., Hu, S. H., Sun, M., Zhao, Z. B., et al. (2001). Geochemistry of lower crustal xenoliths from neogene hannuoba basalt, north China craton: Implications for petrogenesis and lower crustal composition. *Geochimica Cosmochimica Acta* 65, 2589–2604. doi:10.1016/s0016-7037(01)00609-3

Ma, L., Jiang, S. Y., Dai, B. Z., Jiang, Y. H., Hou, M. L., Pu, W., et al. (2013). Multiple sources for the origin of Late Jurassic Linglong adakitic granite in the Shandong Peninsula, eastern China: Zircon U-Pb geochronological, geochemical and Sr–Nd–Hf isotopic evidence. *Lithos* 162–163, 251–263. doi:10.1016/j.lithos.2013.01.009

Ma, L., Jiang, S. Y., Hofmann, A. W., Dai, B. Z., Hou, M. L., Zhao, K. D., et al. (2014). Lithospheric and asthenospheric sources of lamprophyres in the Jiaodong Peninsula: A consequence of rapid lithospheric thinning beneath the north China craton? *Geochimica Cosmochimica Acta* 124, 250–271. doi:10.1016/j.gca.2013.09.035

McDonough, W. F., and Sun, S. S. (1995). The composition of the Earth. *Chem. Geol.* 120, 223–253. doi:10.1016/0009-2541(94)00140-4

Meng, Q. R., Wu, G. L., Fan, L. G., and Wei, H. H. (2019). Tectonic evolution of early Mesozoic sedimentary basins in the North China block. *Earth-Science Rev.* 190, 416–438. doi:10.1016/j.earscirev.2018.12.003

Menzies, M., Xu, Y., Zhang, H., and Fan, W. (2007). Integration of geology, geophysics and geochemistry: A key to understanding the north China craton. *Lithos* 96, 1–21. doi:10.1016/j.lithos.2006.09.008

Peccerillo, A., and Taylor, S. R. (1976). Geochemistry of eocene calc-alkaline volcanic rocks from the Kastamonu area, Northern Turkey. *Contr. Mineral. Pet.* 58, 63–81. doi:10.1007/bf00384745

Rapp, R. P., and Watson, E. B. (1995). Dehydration melting of metabasalt at 8–32 kbar: Implications for continental growth and crust-mantle recycling. *J. Petrology* 36, 891–931. doi:10.1093/petrology/36.4.891

Rapp, R., Shimizu, N., Norman, M., and Applegate, G. (1999). Reaction between slab-derived melts and peridotite in the mantle wedge: Experimental constraints at 3.8 GPa. *Chem. Geol.* 160, 335–356. doi:10.1016/s0009-2541(99)00106-0

Richards, J. P., and Kerrich, R. (2007). Special paper: Adakite-like rocks: Their diverse origins and questionable role in metallogenesis. *Econ. Geol.* 102, 537–576. doi:10.2113/gsecongeo.102.4.537

Rollinson, H. R. (1993). *Using geochemical data: Evaluation, presentation, interpretation*. Singapore: Longman Singapore Publishers (Pte) Ltd.

Sen, C., and Dunn, T. (1994). Dehydration melting of a basaltic composition amphibolite at 1.5 and 2.0 GPa: Implications for the origin of adakites. *Contr. Mineral. Pet.* 117, 394–409. doi:10.1007/bf00307273

Soesoo, A. (2000). Fractional crystallization of mantle-derived melts as a mechanism for some I-type granite petrogenesis: An example from lachlan fold belt, Australia. *J. Geol. Soc. Lond.* 157, 135–149. doi:10.1144/jgs.157.1.135

Song, M.-C., Li, J., Yu, X.-F., Song, Y.-X., Ding, Z.-J., and Li, S.-Y. (2021). Metallogenic characteristics and tectonic setting of the Jiaodong gold deposit, China. *Solid Earth Sci.* 6 (4), 385–405. doi:10.1016/j.sesci.2021.07.002

Sun, S.-s., and McDonough, W. F. (1989). "Chemical and isotopic systematics of oceanic basalts: Implications for mantle composition and processes," in *Magmatism in the ocean basins*. Editors D. Saunders and M. J. Norry (London: Geological Society), 313–345.

Thompson, A. B., Matile, L., and Ulmer, P. (2002). Some thermal constraints on crustal assimilation during fractionation of hydrous, mantle-derived magmas with examples from central alpine batholiths. *J. Petrology* 43, 403–422. doi:10.1093/petrology/43.3.403

Weinberg, R. F., and Hasalová, P. (2015). Water-fluxed melting of the continental crust: A review. *Lithos* 212–215, 158–188. doi:10.1016/j.lithos.2014.08.021

Whitney, D. L., and Evans, B. W. (2010). Abbreviations for names of rock-forming minerals. *Am. mineralogist* 95, 185–187. doi:10.2138/am.2010.3371

Windley, B. F., Maruyama, S., and Xiao, W. J. (2010). Delamination/thinning of sub-continental lithospheric mantle under Eastern China: The role of water and multiple subduction. *Am. J. Sci.* 310, 1250–1293. doi:10.2475/10.2010.03

Wu, F., Yang, J., Xu, Y., Wilde, S. A., and Walker, R. J. (2019). Destruction of the north China craton in the mesozoic. *Annu. Rev. Earth Planet. Sci.* 47, 173–195. doi:10.1146/annurev-earth-053018-060342

Wu, F. Y., Lin, J.-Q., Wilde, S. A., Zhang, X. O., and Yang, J. H. (2005a). Nature and significance of the Early Cretaceous giant igneous event in eastern China. *Earth Planet. Sci. Lett.* 233, 103–119. doi:10.1016/j.epsl.2005.02.019

Wu, F. Y., Yang, J. H., Wilde, S. A., and Zhang, X. O. (2005b). Geochronology, petrogenesis and tectonic implications of Jurassic granites in the Liaodong Peninsula, NE China. *Chem. Geol.* 221, 127–156. doi:10.1016/j.chemgeo.2005.04.010

Wu, F. Y., Yang, Y. H., Xie, L. W., Yang, J. H., and Ping, X. (2006). Hf isotopic compositions of the standard zircons and baddeleyites used in U–Pb geochronology. *Chem. Geol.* 234, 105–126. doi:10.1016/j.chemgeo.2006.05.003

Wu, Y., and Zheng, Y. (2013). Tectonic evolution of a composite collision orogen: An overview on the Qinling-Tongbai-Hong'an-Dabie-Sulu orogenic belt in central China. *Gondwana Res.* 23, 1402–1428. doi:10.1016/j.gr.2012.09.007

Xu, Y., Li, H., Pang, C., and He, B. (2009). On the timing and duration of the destruction of the North China Craton. *Sci. Bull. (Beijing).* 54, 3379–3396. doi:10.1007/s11434-009-0346-5

Xue, D., Wang, H., Liu, Y., Xie, L., and Shen, P. (2017). An improved procedure for the determination of ferrous iron mass fraction in silicate rocks using a schlenk line-based digestion apparatus to exclude oxygen. *Geostand. Geoanal. Res.* 41, 411–425. doi:10.1111/ggr.12164

Yang, F., Santosh, M., and Kim, S. W. (2018a). Mesozoic magmatism in the eastern North China Craton: Insights on tectonic cycles associated with progressive craton destruction. *Gondwana Res.* 60, 153–178. doi:10.1016/j.gr.2018.04.003

Yang, F., Santosh, M., and Tang, L. (2018b). Extensive crustal melting during craton destruction: Evidence from the Mesozoic magmatic suite of Junan, eastern North China Craton. *J. Asian Earth Sci.* 157, 119–140. doi:10.1016/j.jseaes.2017.07.010

Yang, J., Wu, F., Chung, S., Wilde, S. A., and Chu, M. (2004). Multiple sources for the origin of granites: Geochemical and Nd/Sr isotopic evidence from the gudaoling granite and its mafic enclaves, northeast China. *Geochimica Cosmochimica Acta* 68, 4469–4483. doi:10.1016/j.gca.2004.04.015

Yang, K. F., Fan, H. R., Santosh, M., Hu, F. F., Wilde, S. A., Lan, T. G., et al. (2012). Reactivation of the Archean lower crust: Implications for zircon geochronology, elemental and Sr–Nd–Hf isotopic geochemistry of late Mesozoic granitoids from northwestern Jiaodong Terrane, the North China Craton. *Lithos* 146–147, 112–127. doi:10.1016/j.lithos.2012.04.035

Yang, L. Q., Dilek, Y., Wang, Z. L., Weinberg, R. F., and Liu, Y. (2017). Late Jurassic, high Ba–Sr Linglong granites in the Jiaodong Peninsula, east China: Lower crustal melting products in the eastern north China craton. *Geol. Mag.* 155, 1040–1062. doi:10.1017/s0016756816001230

Zhai, M., Guo, J., and Liu, W. (2001). An exposed cross-section of early Precambrian continental lower crust in North China craton. *Phys. Chem. Earth Part A Solid Earth Geodesy* 26, 781–792. doi:10.1016/s1464-1895(01)00127-2

Zhang, Y., Li, J., Zhang, T., Dong, S., and Yuan, J. (2008). Cretaceous to Paleocene Tectono-Sedimentary Evolution of the Jiaolai basin and the Contiguous Areas of the Shandong Peninsula(North China) and Its Geodynamic Implications. *Acta Geol. Sin.* 82, 1229–1257.

Zhao, G. (2001). Palaeoproterozoic assembly of the North China craton. *Geol. Mag.* 138, S0016756801005040–S0016756801005091. doi:10.1017/s0016756801005040

Zhao, G., Sun, M., Wilde, S. A., and Li, S. (2005). Late Archean to Paleoproterozoic evolution of the North China Craton: key issues revisited. *Precambrian Res.* 136, 177–202. doi:10.1016/j.precamres.2004.10.002

Zheng, Y. F., and Gao, P. (2021). The production of granitic magmas through crustal anatexis at convergent plate boundaries. *Lithos* 402–403, 106232. doi:10.1016/j.lithos.2021.106232

Zhu, G., Liu, G. S., Niu, M. L., Xie, C. L., Wang, Y. S., and Xiang, B. (2009). Syn-collisional transform faulting of the Tan-Lu fault zone, East China. *Int. J. Earth Sci.* 98, 135–155. doi:10.1007/s00531-007-0225-8